Degree Project in Applied Physics

Second cycle, 30 credits

Evaluation of Microlenses for Application in Nanolithography

JOKŪBAS STANČIKAS

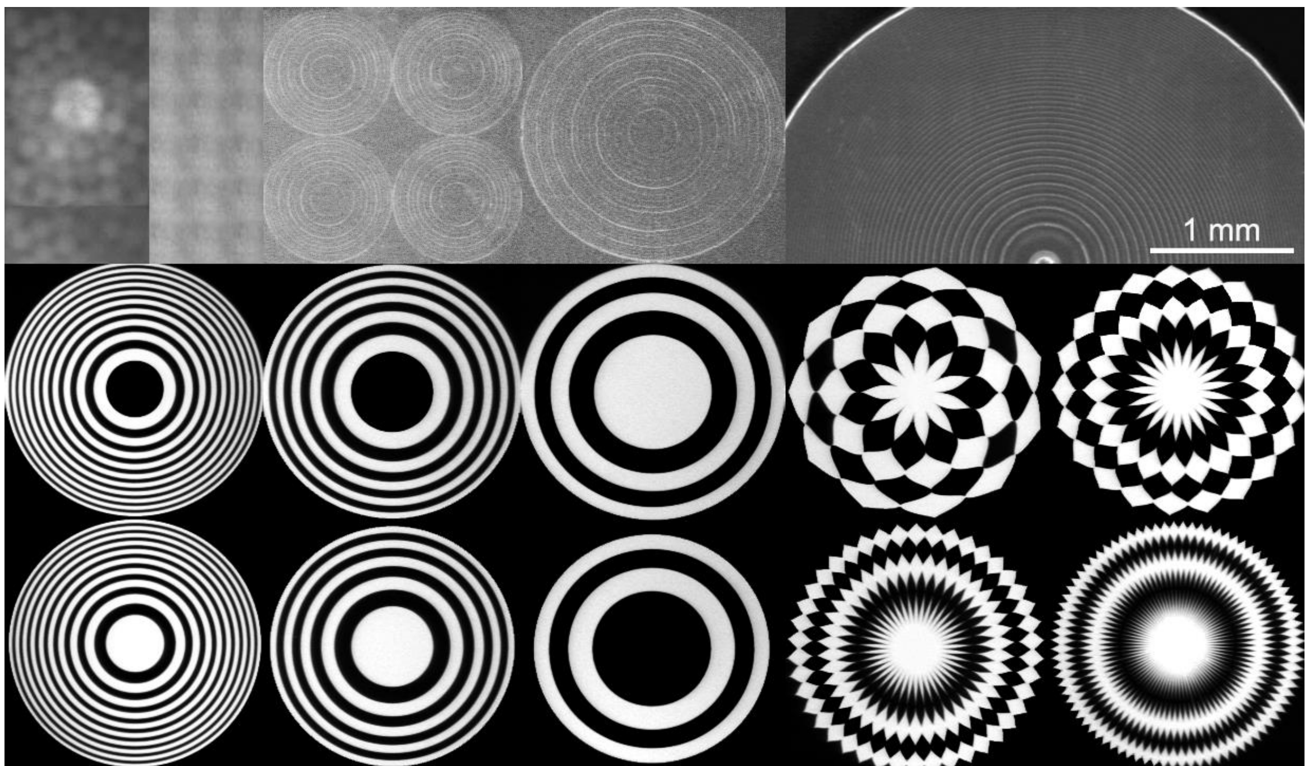

I. Abstract

The topic of this thesis is the evaluation of microlenses (MLs) and microlens arrays (MLAs) for application in nano-lithography, specifically in the context of multibeam laser systems. The problem statement involves finding methods to improve the efficiency and repeatability of a nano-lithographic setup by reducing the number of moving optical elements.

In recent years, advancements in microfabrication and nano-lithography have enabled smaller-scale and more exact optical elements. The biggest barrier to integrating micro-optical elements into lithographic systems is the lack of proper understanding of how well they perform and what effect they have on the quality of the beam, which is crucial to understand for implementation in high-precision optical setups.

To answer these questions, this thesis experimentally evaluates a range of microlenses, including refractive and diffractive optics. The list of tested technologies includes refractive MLAs, diffractive optical elements (DOEs), Fresnel zone plates (FZPs), Gabor zone pates (GZPs), and metamaterial lenses (also known as metalenses).

The list of key measurements includes the evaluation of the M^2 factor, optical losses, and aberrated wavefront distortions. Several different laser beam characterization tools were used for these tasks, including an M^2 beam analyzer, a Shack-Hartmann wavefront sensor (SHWFS), and a beam profiler. The optical properties of each lens type were evaluated in terms of their ability to focus and collimate light.

The results show that DOEs are the best at maintaining great beam quality, with metalenses and reflective lenses displaying slightly worse performance. Fabricated GZPs show much potential, while FZPs are unusable in more real-life applications. This thesis contributes to the field by better understanding the feasibility of using micro-optics in next-generation nano-lithography systems.

Keywords

Microlens arrays, Nano-lithography, Diffractive Optical elements, Zone Plates, M^2 factor, Wavefront aberrations, Diffractive Optics

II. Sammanfattning

Ämnet för denna avhandling är utvärdering av mikrolinser (ML) och mikrolinsarrayer (MLA) för tillämpning i nanolitografi, speciellt beträffande multistrålelasersystem. Probemställningen innebär att hitta metoder för att förbättra effektiviteten och repeterbarheten för en nanolitografisk uppsättning genom att minska antalet rörliga optiska element.

Under de senaste åren har framsteg inom mikrotillverkning och nanolitografi möjliggjort mindre skala och mer exakta optiska element. Det största hindret för att integrera mikrooptiska element i litografiska system är bristen på korrekt förståelse för hur väl de presterar och vilken effekt de har på strålkvaliteten, vilket är avgörande att förstå för implementering i optiska inställningar med hög precision.

För att besvara dessa frågor utvärderar denna avhandling experimentellt en rad mikrolinser, inklusive refraktiv och diffraktiv optik. Listan över testade teknologier inkluderar refraktiva MLA, diffraktiva optiska element (DOE), Fresnel zone plates (FZP), Gabor zone plates (GZP) och metamateriallinser (även kända som metallinser).

Listan över nyckelmätningar inkluderar utvärdering av M^2-faktorn, optiska förluster och vågfrontsaberrationer. Flera olika laserstrålekarakteriseringsverktyg användes för dessa uppgifter, inklusive en M^2-strålanalysator, en Shack-Hartmann-vågfrontssensor (SHWFS) och en strålprofilerare. De optiska egenskaperna för varje linstyp utvärderades i termer av deras förmåga att fokusera och kollimera ljus.

Resultaten visar att DOE är bäst på att bibehålla god strålkvalitet, medan metamateriallinser och reflekterande linser visar något sämre prestanda. Tillverkade GZP visar mycket potential, medan FZP är oanvändbara i mer verkliga tillämpningar. Denna avhandling bidrar till att bättre förstå genomförbarheten av att använda mikrooptik i nästa generations nanolitografisystem.

Nycklelord

Mikrolinsarrayer, Nanolitografi, Diffraktiva Optiska Element, Zonplattor, M^2-faktor, Vågfrontsavvikelser, Diffraktiv Optik

III. Acknowledgments

The activities reported in this master thesis were hosted by the Pattern Generation group at Mycronic AB. I would like to thank the entire group for the warm welcome and support throughout my time in the department. My deepest gratitude goes to Nur Ismail for his supervision, guidance, and support throughout the project. His involvement and insights were crucial to the success of the thesis project.

I would also like to extend my thanks to Prof. Fredrik Laurell and Prof. Lars-Gunnar Andersson from the Applied Physics Department at KTH for their expertise, advice, and close interest in the progress of the project. I am very thankful to Staffan Eriksson, Sales Manager, and Uwe Schmidt, Product Manager at Quantum Design Sweden, for providing the metalens sample characterized in this thesis, which was produced by the MOXTEK, Inc. team, to whom I give a separate thank you for allowing me to evaluate this new and exciting technology.

Finally, I would like to express my gratitude to my colleagues, friends, and family for their support throughout my master's program.

IV. Acronyms

BPP	Beam Parameter Product
BS	Beam Splitter
CCD	Charge-Coupled Device
CMOS	Complementary Metal-Oxide-Semiconductor
CW	Continuous Wave
DOE	Diffractive Optical Element
EFL	Effective Focal Length
FCL	Fiber Coupled Laser
FS	Fused Silica
FZP	Fresnel Zone Plate
GRIN	Gradient-Index
GZP	Gabor Zone Plate
LD	Laser Diode
NA	Numerical Aperture
ND	Neutral Density
ML	Microlens
MLA	Microlens array
OD	Optical Density
PFZP	Phase Fresnel Zone Plate
PM	Power Meter
PMMA	Polymethyl Methacrylate
SHWFS	Shack–Hartmann wavefront sensor
SM	Single-Mode

Table of Contents

1. Introduction ... 1
   1.1 Overview of microlens applications in nano-lithography ... 1
   1.2 Aim of the thesis ... 2
2. Background ... 3
   2.1 Refractive optics ... 3
      2.1.1 Reflection law ... 3
      2.1.2 Refraction (Snell's) law ... 3
      2.1.3 Numerical aperture ... 4
      2.1.4 Polymethyl methacrylate optics ... 4
      2.1.5 Fused silica optics ... 4
      2.1.6 Gradient-index lenses ... 5
   2.2 Wavefronts ... 6
      2.2.1 Shack–Hartmann wavefront sensor ... 6
   2.3 Diffractive optics ... 7
      2.3.1 Diffractive optical elements ... 7
      2.3.2 Fresnel zone plates ... 8
      2.3.3 Suppressing higher-order modes ... 9
   2.4 Metamaterials ... 10
   2.5 Light-matter interaction ... 11
      2.5.1 Reflectance ... 11
      2.5.2 Transmission ... 12
      2.5.3 Absorption (Beer's law) ... 12
      2.5.4 Neutral density filters ... 12
   2.6 Laser basics ... 13
      2.6.1 Laser diodes ... 13
      2.6.2 Gaussian beam ... 13
      2.6.3 Collimated beam ... 14
      2.6.4 M^2 factor ... 14
      2.6.5 Beam ellipticity ... 15
      2.6.6 Spatial filtering ... 15
      2.6.7 Wedge beam splitters ... 16
   2.7 Multi-beam nano-lithography ... 16
   2.8 Optical aberrations ... 16
      2.8.1 Aberration types ... 17
      2.8.2 Zernike polynomials ... 17
      2.8.3 The five Seidel aberrations ... 19
3. Experimental setup and methods ... 22

3.1 Continuous wave laser system 22
3.1.1 Astigmatic beam 23
3.1.2 Single-mode fiber coupling 25
3.2 Characterized microlenses 26
3.2.1 Refractive lenses 27
3.2.2 Diffractive lenses 27
3.2.3 Binary Fresnel zone plates 28
3.2.4 Gabor zone plates 29
3.2.5 Kinoform Fresnel zone plates 29
3.2.6 Metalens 29
3.3 Zone plate manufacturing 30
3.4 Aperture filling 31
3.4.1 Telescope 31
3.4.2 Lens matching 31
3.5 Light interaction with microlenses 32
3.5.1 Small angle power measurement setup 32
3.5.2 Beam splitter power measurement setup 33
3.6 M^2 factor measurement setup 34
3.6.1 Laser reference 35
3.6.2 Focusing lens characterization 35
3.6.3 Microlens characterization 36
3.7 Wavefront measurement setup 37
3.7.1 Laser reference 38
3.7.2 Focusing lens characterization 38
3.7.3 Microlens characterization 38
4. Results 39
4.1 Laser diode properties 39
4.2 Single-mode fiber coupling 40
4.3 Characterized microlenses 40
4.4 Light interaction with microlenses 42
4.4.1 Small angle power measurements 42
4.4.2 Beam splitter power measurements 44
4.4.3 Results comparison 45
4.5 Beam propagation 46
4.6 M^2 factor measurements 48
4.7 Wavefront measurements 50
5. Discussion 53
5.1 Refractive micro-optics 53
5.2 Diffractive micro-optics 53

6. Conclusions 55
6.1 Future work 57
References 58
Appendix 65
A.1 Zernike polynomials 65
A.2 Expanded measurement results 66
A.2.1 Expanded small angle power measurement results 66
A.2.2 Expanded beam splitter power measurement results 67
A.2.3 Light interaction with microlenses. Expanded result comparison 68
A.2.4 M^2 factor measurements for focusing lenses 69
A.2.5 Wavefront measurements 69

1. Introduction

1.1 Overview of microlens applications in nano-lithography

Nano-lithography is an advanced patterning technique that uses photons or electrons to write micro and nanoscale features onto a substrate, commonly used in semiconductor manufacturing. With demand for smaller structures continuing to grow, there is a rise in the need for more efficient high-resolution lithography methods [1]. Traditional lithography systems often rely on moving optical elements such as mirrors, lenses, or even whole optical assemblies [2].

Micro-optics developed as a sub-category of classical optics in the second part of the 20th century [3]. Initially focused on miniaturization of traditional refractive and reflective lenses, as well as novel diffractive optics below 1 mm diameter (down to a few micrometers) while maintaining high surface quality [4]. In recent years, the field has been strongly overlapping with fields of optical microsystems, such as integrated, waveguide optics, active micro-optical components, and MEMS [3].

Refractive and reflective optics are designed according to the laws of geometrical optics [4]. The field covers micromirrors, refractive microlenses (MLs), microlens arrays (MLAs), prisms, beam splitters (BS), etc. The optical function of MLAs is to act as a 2D periodic structure (where the period corresponds to the lens pitch) of individual MLs.

Typical application areas of MLs involve systems where space is a limited resource, and the optical paths, thus effective focal lengths (EFLs), are short [3]. MLAs have even more applications than single MLs, as they can be used for beam homogenization and shaping, Shack-Hartmann wavefront sensors (SHWFS), collimation of light from many small light emitters, fiber coupling, etc. [3, 4, 5].

Diffractive optical elements (DOEs) are based on planar surface-level or embedded micro-structures and are categorized into binary, multilevel, and continuous profile diffractive optics [4]. DOEs involve diffraction and thus interference of light from the different zones forming a desired wavefront [3, 4].

Many fabrication techniques for DOEs involve high-resolution nano-lithography [6], which enables high flexibility and control in the optical design of the MLs. This allows DOEs to replicate functions of a wide variety of optical elements such as lenses, prisms, mirrors, etc. [4].

1.2 Aim of the thesis

The goal of this thesis is to evaluate micro-lenses based on different operational principles and fabrication technologies for their application in nano-lithography experiments. This experimental master's thesis project aims to compare various micro-lenses and technologies, finding those that, based on performance, could be used in the next generation of Mycronic writers.

The application of interest involves using a pair of MLAs to collimate multiple diverging beams into a parallel array of beams. Another identical MLA would then be used to refocus the beams. This optical setup would allow for the translation of the second microlens along the optical axis as shown in Figure 1.1.

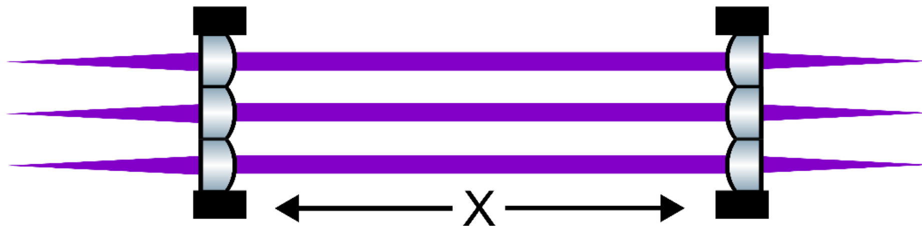

Figure 1.1: Application of MLAs for collimating and refocusing diverging laser beams.

Micro-lenses can operate based on different principles. Most commonly, they rely on refraction, as seen in conventional lenses and graded-index (GRIN) lenses [7]. Another significant sub-category is diffractive lenses, such as FZPs, GZPs, and DOEs, which use diffractive optics and offer several advantages over conventional lenses, along with certain limitations [8].

Moreover, with the rapid advancements in nanofabrication techniques, we are seeing the development of new products based on metamaterials. These materials exhibit exotic properties not found in nature and can be used to create ultra-thin lenses that promise to outperform conventional lenses in terms of reducing distortions and aberrations [7].

In addition to the various operational principles of micro-lenses, they can also be manufactured using different technologies. For example, conventional refraction-based micro-lenses can be produced through 3D printing, molding, or even lithographic techniques [9]. The same holds for other types of micro-lenses. Different manufacturing techniques can affect the overall performance of the lenses [10, 11].

The tasks for the thesis include planning and execution of measurements in the lab. Characterization of the MLs and MLAs using different experimental techniques. Creation of realistic models of the lenses using programming tools such as Zemax and MATLAB. Result analysis, evaluation, and reporting.

2. Background

In this chapter, a brief overview will be given on micro-optics, fabrication techniques, optical and laser basics, and a description of the optical measurement methods that were used in the project. Also, the parameters and principles necessary for understanding the results will be discussed.

2.1 Refractive optics

2.1.1 Reflection law

When rays of light strike the boundary between two different media and reflect, the reflected rays stay within the same plane of incidence. This plane holds both the incident rays and the surface normal to the point of incidence. Additionally, the angle at which the ray reflects θ_r is equal to the angle at which it arrived θ_i [12]:

$$\theta_r = \theta_i \tag{2.1}$$

2.1.2 Refraction (Snell's) law

When rays of light strike the boundary between two transparent media of different refractive indices n_i and n_t the rays are split into two portions, reflected ones that follow the previously covered reflection law and refracted (or transmitted) rays. The refracted rays stay within the plane of incidence, while the angle of refraction θ_t is related to the angle of incidence θ_i according to the law of refraction (or Snell's law) [13]:

$$n_i \sin \theta_i = n_t \sin \theta_t \tag{2.2}$$

2.1.3 Numerical aperture

In an optical system, the numerical aperture (NA) describes its angular acceptance of incoming light [14]. With the increase in magnification, the EFLs and diameter of the objective lenses decrease proportionally, and so does the solid angle of useful rays from the object. This relation is defined as the product of the refractive index and the sine of the half-angle [12].

$$NA = n\sin(\alpha) \tag{2.3}$$

2.1.4 Polymethyl methacrylate optics

Polymethyl methacrylate (PMMA) MLs and MLAs are fabricated by using injection molding, modified LIGA process, photoresist reflow process, or hot embossing methods [15, 10, 11].

Injection molding is the fastest and thus most cost-effective method to produce MLAs. During this process melted PMMA is directly injected into a mold holding an MLA-shaped nickel electroplated cavity [10].

During hot embossing a patterned mold of bulk metallic glass is pressed at pressures in the range of 2 MPa into heated PMMA, at temperatures of 120 - 140 °C imprinting the MLA shape [15].

LIGA process (German acronym for lithography, electroforming, and molding) is a method well suited for the manufacturing of microdevices with high aspect ratios. This process is based on the physical change of the characteristic glass transition temperature (T_g) when exposed to X-rays. Typical LIGA procedure includes exposing PMMA to x-rays, development, second exposure, and thermal treatment. Under exposure to x-rays PMMA polymers transition from a rubber into a glass state, and surface tension during reflow forms a lenslet [11].

Mentioned methods have been shown to produce MLs and MLAs with diameters of as low as 30 μm with a surface roughness of less than 10 nm [15, 10, 11].

2.1.5 Fused silica optics

Fused silica (FS) MLs and MLAs are fabricated by using methods such as photolithography [16], reflow or melting of resist technique [17], and reactive ion etching [9].

Similarly to PMMA MLs, photolithography, followed by a reflow or melting of the resist allows for the fabrication of convex aspherical FS MLs and MLAs. The process starts by forming a photoresist ML, which involves patterning polymer cylinders on a substrate surface, and reflowing the formed photoresist under 170 – 200 °C the temperature. This formed sample is then transferred to another (i.e., FS) substrate by reactive ion (dry) etch process [16, 17].

A simple method to fabricate concave MLs involves modifying the FS substrate with a pulsed CO_2 laser, this localized modification has higher selectivity and acts as a starting point for the wet-etching process, during which hydrofluoric (HF) acid is used to etch a valley inside the substrate, which then can be used as a concave lens [9].

Similarly, MLs and MLAs of desired shape can be formed through the selective laser etching (SLE) process which involves introducing type II modifications (i.e. nano gratings) in the volume of a glass material such as FS using a laser system equipped with 3D (XYZ) nano positioning stage and an ultra-short pulsed laser source (~ 700 fs, with a pulse repetition rate of 610 kHz). The modified glass regions have increased selectivity (up to 700x of the unmodified material) for etchants such as HF acid or heated (up to 95 °C) potassium hydroxide (KOH) solution. This allows modified regions to be etched at an increased rate, while the unmodified material stays close to its original dimensions. The shape of the desired micro-optic device can be designed according to the user's specifications, which makes this technique very flexible [18, 19].

Mentioned methods have been shown to produce MLs and MLAs with diameters of as low as 30 μm [16, 9], and with a surface roughness in the range of 1 nm [9].

2.1.6 Gradient-index lenses

In traditional refractive lenses, varying delay of the optical phase of the beam is introduced by varying the curvature and thickness of the lens material. Gradient-index (GRIN) lenses offer the same effect while keeping the thickness of the lens constant but varying the material's refractive index radially [20], with a schematic diagram of the GRIN lenses' effect on light rays shown in Figure 2.1.

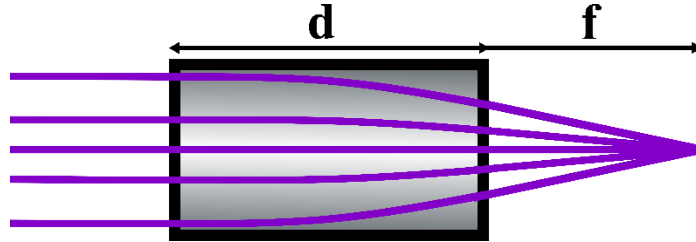

Figure 2.1: Schematic diagram of a GRIN lens and ray path through it.

GRIN lenses can be explained through the application of Snell's law to a continuous refractive index change in the Y-axis, which is perpendicular to the propagation direction Z, according to the following paraxial wave equation [3]:

$$n^2(y) = n_{max}^2(1 - \alpha^2 y^2) \tag{2.4}$$

where max value n_{max} is at $y = 0$ and α is the grading constant. If $\alpha^2 y^2 \ll 1$, then we get:

$$n(y) \approx n_{max}(1 - \frac{1}{2}\alpha^2 y^2) \tag{2.5}$$

Which corresponds to a parabolic index of refraction change in the Y-axis [3].

GRINs are common the laser printers, photocopiers, imaging, microscopy, and fiber optic systems [7, 20, 21]. The main advantage of such optical elements is that they allow for the control of aberrations through the optical design of the materials.

Small-diameter GRINs are typically fabricated via an ionic diffusion process [7]. A homogenous glass material is submerged inside molten salt for multiple hours during which ionic exchange occurs. The effect is radial, as outwards regions are closer to high-concentration ion source. This gradient in ion concentration results in a gradient of refractive index, which achieves a lens effect [7, 21].

Concave or convex lens counterparts can be fabricated depending on the relative refractive index of the glass material before and after the ionic diffusion process. This can be controlled during the choice of the glass and salt materials [22, 7].

2.2 Wavefronts

A light wave at a specific point in space can be described by its frequency, amplitude, and direction of propagation. However, this info doesn't offer much of an insight on the optical aberrations across a wider area [7]. To understand these spatial disturbances a concept of a wavefront is used, which is described as a surface connecting all points that are in the same phase of a monochromatic light waves [23].

Types of optical wavefronts include plane wavefronts, which are characteristic to collimated light sources and sources at an infinite distance, spherical wavefronts, which are made up of concentric spheres expanding outward from a point source, aberrated wavefronts, resulting from optical imperfections, Gaussian wavefronts, which are characteristic of laser beams, etc. [7, 24].

2.2.1 Shack–Hartmann wavefront sensor

To measure the wavefront of an incoming light source Shack-Hartmann wavefront sensor is the most popular choice. The device is highly versatile in its applications ranging from laser beam analysis and optical telescope alignment to adaptive optics systems.

A Shack-Hartmann wavefront sensor consists of an MLA and an image sensor found at the focal plane of the MLs. Each lenslet focuses light onto a separate part of the sensor. The position of each focal spot corresponds to the averaged wavefront orientation over the area of the lenslet. Considering all the values from each lenslet, the wavefront can be imaged, and distortions can be estimated [25].

Schematic representation of Shack-Hartmann wavefront sensor principles are shown in Figure 2.2, with (a) showing an example of flat wavefront measurement, and its image on the sensor, and (b) showing a measurement of a distorted wavefront.

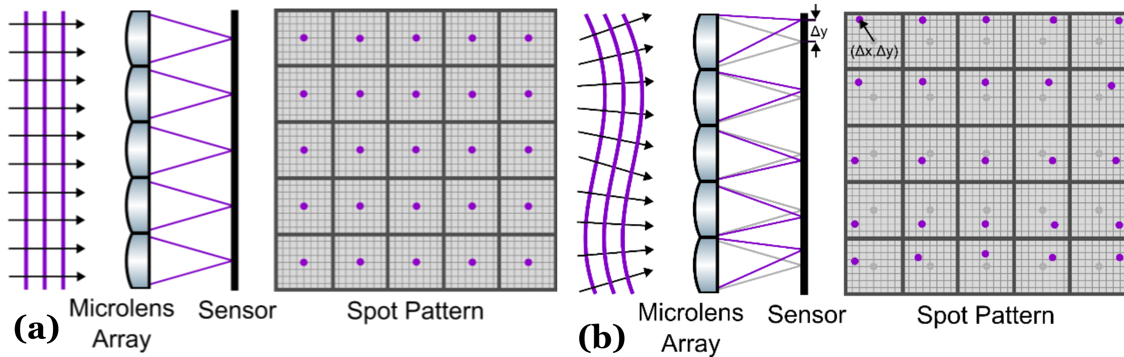

Figure 2.2: Schematic of Shack-Hartmann wavefront sensor principles: (a) flat wavefront and (b) wavefront distorted by optical aberrations, with corresponding spot patterns shown on the right.

2.3 Diffractive optics

Diffractive optics guide light through diffraction, using micro-scale patterns to alter the phase of the incoming light wave and cause them to bend around the edges of an obstruction [12]. Diffraction can be explained using Huygens' wave principle. According to this every point on a wavefront acts as a source of secondary wavelets that generate another plane wavefront. When a part of the wavefront is blocked by a slit it bends at the edges [26].

The Rayleigh criterion is a useful parameter used to describe small-scale diffractive systems. A system that meets this condition has its performance controlled by the wave properties of light and is called a diffraction-limited system [8]. It defines the minimum angular separation at which two-point sources cannot be distinguished:

$$\theta = 1.22\frac{\lambda}{d} \tag{2.6}$$

Where θ is the angular resolution, λ is the wavelength of light, and d is the diameter of the aperture [7].

2.3.1 Diffractive optical elements

Diffractive optical elements (DOEs) are complex diffractive devices that can be seen as special apertures and can be optically engineered to obtain a desired intensity and phase profile at the plane of interest. This enables thinner designs with feature sizes from a few hundred nanometers to a few millimeters, custom to the task, and of smaller scale than refractive lenses. Extremely fine feature patterns, which are smaller than the diffraction limit can be fabricated using

ultraviolet lithography, electron beam lithography, and focused ion beam lithography [26].

2.3.2 Fresnel zone plates

Fresnel zone plate (FZP) is a form of basic DOE, which can be used to focus light. Three main categories for FZP are binary, multi-layer, and kinoform FZPs, as shown in Figure 2.3 (the codes used to produce these figures were based on examples given in *"Design and Fabrication of Diffractive Optical Elements with MATLAB"* [26]).

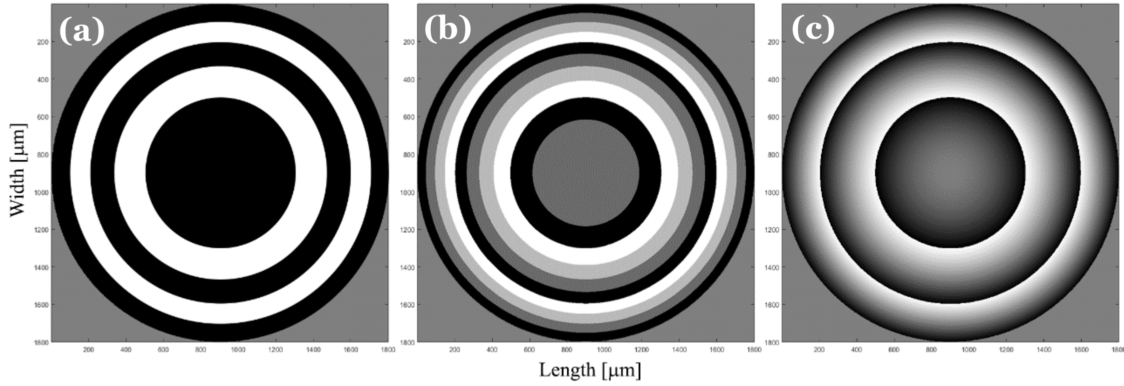

Figure 2.3: Different Fresnel zone plate designs tailored for a 405 nm wavelength, featuring a 400 mm effective focal length and a 900 μm aperture radius. The variations include (a) F4N - a binary FZP (b) a four-level FZP, and (c) a kinoform FZP [26].

To express the electric field at an observation point P, a Rayleigh-Sommerfeld diffraction integral of the first kind can be used [27]:

$$E(P) = \frac{1}{2\pi} \iint_{S_A} E(\vec{r}) \frac{e^{jkr}}{r^3} z_p (jkr - 1)\, dS \tag{2.7}$$

where $E(\vec{r})$ stands for the electric field at a point $\vec{r}$ on the aperture, r is the distance between the observation point and the point on the aperture, and z_p is a parameter representing the projection along the observation axis. The term $(jkr - 1)$ describes the phase and amplitude modification due to the propagation. This integral form accounts for the complex behavior of diffraction, capturing both the near-field and far-field characteristics without approximations [27].

For a simple case involving light with a flat wavefront, a binary FZP can be designed for selected EFL with a series of concentric rings (called Fresnel zones), which alternate between transparent and opaque regions. These zones are engineered in a way that light is diffracted from each one constructively interferes at a focal point [28]. To achieve this the radius of the nth zone must satisfy the following condition:

$$R_N = \sqrt{\left(f_1 + \frac{N\lambda}{2}\right)^2 - f_1} \tag{2.8}$$

where R_N is the radius of the n-th zone, f_1 is the EFL of the first order diffraction, N is the number of the zone, λ is the wavelength of the light [27].

For simple binary FZP there are other largest irradiance points of higher-order diffraction along the optical axis. These EFLs can be found at:

$$f_m = \left(\frac{1}{2m-1}\right)\frac{R_1^2}{\lambda} = \left(\frac{1}{2m-1}\right)f_1, \qquad m = 1,2,3,\ldots \tag{2.9}$$

where f_m is the EFL of m-th order diffraction, m is the mode of diffracted light waves. According to this equation we see that focal points occur along the optical axis at points [27]:

$$z_p = f_1, \frac{f_1}{3}, \frac{f_1}{5}, \ldots, \frac{f_1}{2m-1} \tag{2.10}$$

To improve performance of the FZPs, the first change involves changing the opaque zones into transparent ones with thickness that will give rise to an added phase shift of π radians, and would constructively contribute, rather than losing their energy by reflection, scattering or absorption. Such an element is called phase Fresnel zone plate (PFZP). [29].

2.3.3 Suppressing higher-order modes

To combat multi-order behavior of binary FZPs we can force most of the light into a single diffraction order (typically the 1st one) [12]. This is done by changing the pattern and/or geometry of the Fresnel zones, and a couple of methods exist [29].

The Gabor zone plate (GZP) suppresses the higher-order foci to a single focus at:

$$f = \frac{R_1^2}{\lambda} \tag{2.11}$$

It is a difficult DOE to fabricate as it requires sinusoidal transmission in each zone [30]. Therefore, a binary GZP has been developed which introduces an azimuthal and radial variation of the transmittance. It is a popular alternative to the conventional FZPs as it allows for traditional fabrication methods used in FZP manufacturing while suppressing higher-order modes [31].

A more straightforward approach involving change of patter geometry is multi-level (or multi-layer) FZP design (like shown in Figure 2.3b). In 4-level FZP,

Fresnel zones can be designed for the phase delay values of $0, \frac{\pi}{2}, \pi$, and $\frac{3\pi}{2}$. Inside each such area, the profile changes gradually, with a sharp change between the zones [26].

Another more complex version is kinoform design (like shown in Figure 2.3c) constructing a lens using triangular Fresnel prisms. This design yields high efficiency of suppressing higher-order diffraction, however, due to its' complex geometry it is also the more difficult one to manufacture [26, 29]. Kinoform phase patterns that are quantized into Fresnel zones of differing heights in theory should achieve a diffractive efficiency of over 99 % [32].

2.4 Metamaterials

From Maxwell's Equations we see that the refractive index of a material is dependent both on the electric permittivity and the magnetic permeability according to:

$$n \equiv \frac{c}{v} = \pm\sqrt{\frac{\epsilon\mu}{\epsilon_0\mu_0}} \tag{2.12}$$

Where c is the speed of light vacuum, v is speed of light inside of media, ϵ is the electric permittivity and μ is magnetic permeability in vacuum, while ϵ_0 is magnetic permeability inside and μ_0 is magnetic permeability inside of a media. As the definition suggests, the index of refraction can hold both positive and negative value. In 1968, Victor G. Veselago analytically showcased that if a material simultaneously had both $\epsilon < 0$ and $\mu < 0$, its' refractive index n could have a negative value.

At the end of 20th century this led to fabrication of 3D nanostructures consisting of tiny conducting antennas that scatter the electric field. These composite materials are called metamaterials, which above their resonant frequencies show negative indices of refraction. Negative-index media are also known as left-handed materials as the phase velocity moves in the opposite direction to the cross-product of the electric and magnetic fields, like determined by the right-hand rule [7].

More generally metamaterials are fabricated nano-structured materials composed of the building blocks of which size and spacing of atoms are at sub-wavelength scale and their atypical electromagnetic behavior is determined by the size, shape and arrangement of the unit cells, not by chemistry [33]. Some interesting optical properties of engineered metamaterials apart from negative refractive index include, invisibility cloak effect, artificial chirality, superlensing and hyperbolic dispersion relation [33, 34].

One of metamaterial application areas is metamaterial lenses (also known as metalenses) designed for beam shaping or collimation [35]. A common

limitation of superlenses, hyperlenses, and perfect lenses, is the inability to focus a plane wave into a spot as they have no phase compensation mechanism, which would support a plane wave focusing and Fourier transform function. For metalenses a plane wave focusing becomes available by introducing a phase compensation mechanism and using coupling between the metamaterial and air [33]. This phase profile compensates for the differences in optical path distance and ensures that all parts of the wavefront focus on the same point or form the desired optical pattern [34].

For IR applications metalenses use metamaterials such as Silicon (αSi), SiO_2, Si_3N_4 nano-pillars [35, 36]. For visible wavelength range applications niobium oxide (Nb_2O_5), Aluminum nano-pillars are often used [35, 37]. In the past couple of decades, metamaterials with diverse designs and structures have been investigated and have shown many distinct types of lenses which can overcome diffraction limit. However, metamaterials still hold some major limitations such as high losses, deep nanoscale fabrication issues, a rather narrow range of frequencies, angle and polarization dependency, low flexibility of materials and size, and complex integration with the conventional optics components [33].

2.5 Light-matter interaction

The four major ways in which light interacts with matter are reflection, transmission, absorption, and emission [38].

Intensity of light is a measure of energy per time P and area S, averaged over one period of the oscillating electric field, for a wave propagating in a vacuum [5]:

$$I = \frac{P}{S} = \frac{1}{2} c \epsilon_0 n |E_0|^2 \tag{2.13}$$

measured in [W/m^2], where c is the speed of light (3×10^8 m/s), ϵ_0 – vacuum permittivity (8.854×10^{-12} C/(Vm)), n – refractive index of the propagation media, and $|E_0|^2$ – strength of the electric field at a particular point [5].

2.5.1 Reflectance

When light hits an interface of two different transparent media, it is partially transmitted and partially reflected into the original media as described in 2.1.1 Reflection law section [5]. The ratio of reflected light I_r and incident light I_i is called the intensity reflection coefficient R (or reflectance) [39]:

$$R = \frac{I_r}{I_i} = \left(\frac{n_1 - n_2}{n_1 + n_2}\right)^2 \tag{2.14}$$

where n_1 is the refractive index of the original media, and n_2 is the refractive index of the incident media [5].

Due to surface roughness, part of the light is scattered diffusely without wavelength change through elastic scattering, specular and diffuse reflections [39].

2.5.2 Transmission

The part of the light that is not reflected or scattered is transmitted through the media. Transmission coefficient T (or transmittance) relates transmitted light intensity I_t and incident light I_i through the following ratio [38]:

$$T = \frac{I_t}{I_i} \tag{2.15}$$

Due to the absorption, the transmission coefficient T is sensitive to the thickness of the media d it travels through [39].

2.5.3 Absorption (Beer's law)

As a plane wave propagates through a medium along the Z-axis stimulated absorption and emission processes can change its amplitude [38]. This change in light intensity is related trough the linear absorption coefficient α, by assuming that the rate at which the intensity decreases over a small distance dz is directly proportional to the intensity I at that point:

$$I = I(Z) = I_0 e^{-\alpha z} \tag{2.16}$$

this equation is called Beer's law [39].

2.5.4 Neutral density filters

Neutral density (ND) filters are designed to reduce the intensity of light in a range of wavelengths uniformly. Optical density (OD) is an optical parameter used to describe the amount of energy blocked by the filter. High optical density corresponds to a low coefficient of transmission according to the following relation [40]:

$$T = \frac{I_t}{I_i} = 10^{-OD} \tag{2.17}$$

$$OD = -\log\left(\frac{I_t}{I_i}\right) \tag{2.18}$$

Where I_i is incoming and I_t – the transmitted light intensity. To calculate the total OD of a system OD factors are added together [40]:

$$OD_{Total} = OD_1 + OD_2 + \cdots + OD_n \tag{2.19}$$

2.6 Laser basics

The word LASER is an acronym for Light Amplification by Stimulated Emission of Radiation [41]. A laser is an optical device that emits a coherent beam of light at a very narrow wavelength range [24].

2.6.1 Laser diodes

Laser diodes (LDs) are a category of electrically pumped semiconductor lasers. The optical gain is generated by flowing an electric current through a p-n or a p-i-n junction [42]. In these structures, electrons and holes recombine, emitting energy in the form of photons. This process can occur spontaneously or be stimulated by incoming photons, which leads to optical amplification [24].

Most LDs are designed as edge-emitting lasers, where the laser resonator is formed by the facets of the semiconductor wafer [42]. These lasers typically use a double heterostructure. This confines the carriers in a small region while acting as a waveguide for the photons [43]. Often the edge-emitting LDs' active cross-sectional area is rectangular, with the width and height of the emitter varying by orders of magnitude [44].

In recent LD designs, surface-emitting types have been developed, where the laser emission occurs perpendicular to the wafer surface [42].

2.6.2 Gaussian beam

A usual form of a laser beam is Gaussian. Such beam displays minimal angular spread for a given beam waist, which makes it diffraction-limited. This beam type keeps the lowest uncertainty in photon position and propagation direction. This makes it well-localized along the axis of propagation [24]. The intensity distribution of a Gaussian beam follows a Gaussian function, peaking at the central and gradually decreasing radially in a bell-shaped curve [45].

The beam radius $\omega(z)$ and curvature of a wavefront $R(z)$ evolve as the beam propagates. The Rayleigh length z_R stands for the distance from the beam waist to the point where the beam radius increases by $\sqrt{2}$. The beam radius at any z point is given by:

$$\omega(z) = \omega_0 \sqrt{1 + \frac{z_R^2}{z^2}} \tag{2.20}$$

where ω_0 is the beam waist radius at $z = 0$, and z_R - Rayleigh range defined by:

$$z_R = \frac{\pi \omega_0^2}{\lambda} \tag{2.21}$$

The Gaussian beam's divergence angle θ shows how much the beam spreads

as it propagates. It is inversely proportional to the waist size, given by:

$$\theta = \frac{\lambda}{\pi\omega_0^2} \tag{2.22}$$

This relationship between beam waist and divergence highlights an important feature of Gaussian beams, where smaller beam waists lead to larger divergence angles and vice versa. At the smallest waist position, the wavefront is planar, and the beam behaves like a plane wave. As it propagates, the wavefront curvature increases and becomes spherical in the far field [24, 45].

2.6.3 Collimated beam

A collimated beam is characterized by low beam divergence and light rays propagating parallel to each other. This can be achieved by focusing the beam at infinity, leading to a relatively constant beam width. Collimated beam width can be related through Rayleigh length according to the following equation [46]:

$$\omega_{col} = \theta d = \frac{\lambda}{\pi\omega_0} f \tag{2.23}$$

2.6.4 M² factor

The M² factor (otherwise beam quality factor) is a metric used to describe how closely a real laser beam approximates an ideal Gaussian beam [47]. For an ideal Gaussian beam ($TEM_{00\,mode}$), the beam parameter product (BPP - the product of the divergence angle and beam waist radius) is minimal [48]. Real beams tend to differ from an ideal beam due to optical imperfections, beam aberrations, etc., leading to larger BPPs [24]. The M² factor expresses this deviation of BPPs as [48]:

$$M^2 = \frac{BPP(real\ beam)}{BPP(ideal\ Gaussian\ beam)} = \frac{\pi\theta\omega_0}{\lambda} \tag{2.24}$$

For an ideal Gaussian beam, $M^2 = 1$, a higher M^2 value shows worse beam quality. This means the beam has higher divergence and thus is harder to focus [24]. A lower value than 1 is physically not possible [47].

The BPP can be expressed as relation M2 factor with wavelength λ as [49]:

$$BPP = \varphi\omega_0 = M^2\frac{\lambda}{\pi} \tag{2.35}$$

For example, LDs typically have M^2 values between 1.1 and 1.7, showing they produce non-ideal beam profiles. High M^2 values make the beam more difficult to work with, often requiring more optical solutions [50].

2.6.5 Beam ellipticity

Diffraction is stronger when the dimension of the aperture is smaller [24]. The different aperture‘s dimensions in edge-emitting LDs result in different beam divergence angles and produce the characteristic elliptical beams. The divergence angles of the parallel (θ_{slow}) and perpendicular (θ_{fast}) orientations differ ($\theta_{slow} < \theta_{fast}$) [44]. Ellipticity can be related through the ratio of the difference between the major axis radius and the minor axis radius divided by the major axis radius [51]:

$$f = \frac{Half\ major\ axis - Half\ minor\ axis}{Half\ major\ axis} = \frac{r_1 - r_2}{r_1} \tag{2.26}$$

To circularize such a beam a pair of cylindrical lenses can be used. This is done by expanding the narrower (θ_{slow}) axis of the beam by selecting a pair of cylindrical lenses according to the following equation:

$$\theta_{fast} = \theta_{slow} \frac{f_2}{f_1} \tag{2.27}$$

Where f_1 and f_2 are the EFLs of the two cylindrical lenses [51]. An example displaying a beam expander is shown in Figure 2.4.

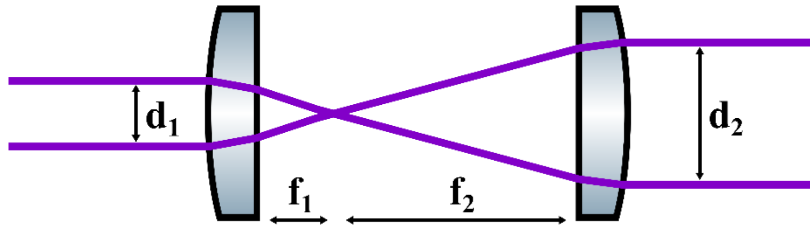

Figure 2.4: Schematic diagram of a beam expander using a pair of cylinder lenses with ELFs f_1 and f_2 used to increase collimated beam diameter (from d_1 and d_2) in one dimension.

2.6.6 Spatial filtering

Spatial filters are used in laser optical systems to improve the beam quality by removing unwanted multiple-order energy peaks and allowing only the central maximum of the diffraction patter to propagate. A pinhole aperture is capable of spatial filtering in an optical system by placing it at the focal point withing the system. Optimal pinhole diameter, where around 99.3 % of light is transmitted, can be found using the following equation [52]:

$$D = \frac{\lambda f}{\omega_0} \tag{2.28}$$

Single-mode (SM) fibers play a critical role in laser systems, as spatial filters that improve beam quality (and thus M^2 factor) by eliminating higher-order spatial

modes and allowing only the fundamental mode to propagate [53].

An SM fiber supports only the fundamental mode (HE_{11}) propagation when the normalized frequency parameter V is less than 2.405. This is called the single-mode condition:

$$V = \frac{2\pi a}{\lambda} \sqrt{n_{core}^2 - n_{cladding}^2} < 2.405 \tag{2.29}$$

where a is the core radius, λ is the wavelength of light, n_{core} refractive index of core, and $n_{cladding}$ refractive index of the cladding [54].

2.6.7 Wedge beam splitters

Wedge beam splitters (BS) are simple optical elements with a prism geometry and made of a transparent material with a small apex angle (in the range of 1°). When a beam enters the BS, the beam undergoes multiple internal reflections. As the two surfaces of the prism are not parallel, each internal reflection between the surfaces introduces a cumulative angular deviation. This feature of the BS is handy, as the first transmitted beam, which passes through without any internal reflections, follows a different path from the other beams that experience internal reflections. This allows to separate the beams more easily [55].

2.7 Multi-beam nano-lithography

Nano-lithography is an advanced patterning technique using photons or electrons to write nanoscale features onto a substrate. Three main categories involve maskless photolithography, image projection, and focal spot writing [1].

Multi-beam laser pattern generators are common in microelectronics fabrication, where speed is a relevant issue [2].With the increase in complexity of RET (resolution enhancement technology) masks, multi-beam writers became the preferred choice. Multi-beam nano-lithography is a class of optical maskless photolithography [56]. Nano-lithography systems based on multi-beam pattern generators use multiple parallel individually controlled laser beams to expose specific areas. This improves both the throughput and resolution of a system, making it ideal for high-precision applications in nanotechnology and semiconductor manufacturing writing with nano-scale accuracy [1].

2.8 Optical aberrations

In optics imagining system properties causes different kinds of optical aberrations, which are imperfections affecting the wavefront of the light waves and can be analyzed with geometrical (ray) optics [57]. We typically consider a perfect optical wavefront to be flat, meaning all the propagating parallel light waves are in phase with each other. Any aberrations introduced into the optical path will distort this wavefront, causing different parts of the light to go out of phase. These

aberrations effectively reduce the beam quality, leading to decreased focusing precision and poorer imaging performance. Many of the aberrations can be fully predicted using Snell‘s law. Often, they are caused by the inability of the optical surfaces to refract or reflect rays from an object to a single (or correct intended) image point. Therefore, often they do not originate from poorly made optical components but are inherent to the geometry of the used optical elements [58].

A simple expression for optical aberrations states that the inverse output curvature s' is equals to sum of inverse input curvature s and inverse added curvature f [8]:

$$\frac{1}{s'} = \frac{1}{s} + \frac{1}{f} \tag{2.30}$$

If the aberrations are larger than the theoretical diffraction pattern, the image will be dominated by aberration effects, we call this aberration-limited optical system. If the point aberrations are smaller than the diffraction pattern, the image will be dominated by the diffraction effects, such system is called diffraction-limited optical system [58].

2.8.1 Aberration types

There are also two general types of aberrations related to the frequency of light:

- Chromatic aberrations that arise from dispersion, meaning that index of refraction for most materials is dependent on the wavelength of light. This can lead to EFL of an optical element depending on the wavelength of light.
- Monochromatic point aberrations and field aberrations. These two sub-categories of monochromatic aberrations are related to the performance of focusing to a single point:
  - Point aberrations involve rays from a single point in the object space that do not converge to a single point in the image space [58]. For example, spherical aberration, coma, and astigmatism [7].
  - Field aberrations (or aberrations of the image shape) occur when rays from a point in the object space do converge to a single point in the image space, but that point is not at the ideal (paraxial) image position. This means that while each point is sharply imaged, their locations are shifted from a flat plane [58]. For example, distortion and Petzval field curvature [7].

2.8.2 Zernike polynomials

The Zernike polynomials consist of a series of polynomials with the coefficients of each polynomial showing the magnitude of each type of Zernike aberration present in the optical wavefront aberration map. This allows expressing numerically what particular type and magnitude aberration is prese [59].

Zernike polynomials can be simply written in polar coordinates as products of angular functions and radial polynomials. Mathematically they are defined by:

$$\begin{cases} m \neq 0 & \begin{cases} Z_{even\ j} = \sqrt{2(n+1)}R_n^m(r)\cos m\theta \\ Z_{odd\ j} = \sqrt{2(n+1)}R_n^m(r)\sin m\theta \end{cases} \\ & m = 0 \quad Z_j = \sqrt{n+1}R_n^m(r) \end{cases} \tag{2.31}$$

where

$$R_n^m(r) = \sum_{k=0}^{\frac{n-m}{2}} \frac{(-1)^k (n-k)!}{k!\left[\frac{n+m}{2}-k\right]!\left[\frac{n-m}{2}-k\right]!} r^{n-2k} \tag{2.32}$$

The indices n corresponds to the radial degree and m - to the azimuthal frequency, while j stands for the mode-ordering number. Table 2.1 shows the relationships among these indices for the first ten most common (0th to 3rd order) modes [60].

Table 2.1: Zernike Polynomials from radial orders n 0 to 3. Displayed with frequency m, and their relation to ocular aberrations (expanded table shown in Appendix section A.1 Zernike polynomials) [59].

n	**m**	$\mathbf{Z_n^m}$	$\mathbf{Z_n^m}$ **(p, θ)**	**Title**
0	0	Z_0^0	1	Piston
1	−1	Z_1^{-1}	$4^{1/2}$ p sinθ	Tilt (about x-axis, horizontal tilt)
1	1	Z_1^1	$4^{1/2}$ p cosθ	Tilt (about y-axis, vertical tilt)
2	−2	Z_2^{-2}	$6^{1/2}$ p² sin2θ	Astigmatism (axis 45°, 135°)
2	0	Z_2^0	$3^{1/2}$ (2p² – 1)	Spherical defocus
2	2	Z_2^2	$6^{1/2}$ p² cos2θ	Astigmatism (axis 0°, 90°)
3	−3	Z_3^{-3}	$8^{1/2}$ p³ sin3θ	Trefoil (base on x-axis)
3	−1	Z_3^{-1}	$8^{1/2}$ (3p³ – 2p) sinθ	Coma (along x-axis)
3	1	Z_3^1	$8^{1/2}$ (3p³ – 2p) cosθ	Coma (along y-axis)
3	3	Z_3^3	$8^{1/2}$ p³ cos3θ	Trefoil (base on x-axis)

These polynomials are used because of their mathematical properties, as all their derivatives are continuous, they efficiently represent common optical aberrations (e.g., coma, spherical aberrations), and they form a complete orthonormal set over a unit circle [8].

Some of the properties for the polynomials include:

- The indices n and m are always integers and satisfy:

$$\begin{cases} m < n \\ n - m = \text{even} \end{cases} \tag{2.43}$$

- The polynomials keep their form unchanged when the coordinate axes are rotated around the center of the pupil.

$$R_n^m(r) = R_n^{-m}(r) \tag{2.34}$$

$$\int_0^1 R_n^m(r) R_{n'}^m(r) r dr = \frac{\delta nn'}{2(n+1)} \tag{2.35}$$

$$\int d^2 r W(r) Z_j(r) Z_{j'}(r) = \delta jj' \tag{2.36}$$

where

$$W(r) = \begin{cases} \frac{1}{\pi} & for \ \ |r| \leq 1 \\ 0 & for \ \ |r| > 1 \end{cases} \tag{2.37}$$

is the weighting function [60].

The wavefront aberration $W(p\theta)$ (indicating the optical path length versus position in two dimensions) is broken down into a sum of Zernike polynomials, as represented by the following formula [57, 58]:

$$W(p\theta) = \sum\nolimits_{nm} C_n^m Z_n^m(p\theta) = C_0^0 Z_0^0 + C_1^{-1} Z_1^{-1} + C_1^1 Z_1^1 + C_2^{-2} Z_2^{-2} + \cdots \tag{2.38}$$

2.8.2.1 Chromatic aberration

As described previously chromatic aberration rises from dispersion, meaning that index of refraction for material is dependent on the wavelength of light. Due to chromatic aberrations the refractive power $K(\lambda)$ of a thin lens will become dependent on the wavelength of light λ:

$$K(\lambda) = [n(\lambda) - 1]\left(\frac{1}{R_1} - \frac{1}{R_2}\right) \tag{2.39}$$

which shows that the EFL $f(\lambda)$ for a thin lens will be wavelength-dependent as well (i.e. a lens with $R_2 = -R_1$) [58]:

$$f(\lambda) = \frac{R_1}{2}\frac{1}{n(\lambda) - 1} \tag{2.40}$$

2.8.3 The five Seidel aberrations

Monochromatic aberrations in rotationally symmetric optical systems can

be divided into five main types. These primary aberrations are also known as Seidel aberrations and include the following aberration types [57].

Another notation for the aberration polynomial that includes the sum of terms such as various power of the pupil and image coordinates (i.e., x, y, ξ, η), each term with its own coefficient in form of a_{ijkl}. Such polynomials and its first rems can be expressed:

$$W(x,y,\xi,\eta) = \sum_i \sum_j \sum_k \sum_l a_{ijkl}\, x^i\, y^j\, \xi^k \eta^l \\ = a_{0000} + a_{1000}x + a_{0100}y + a_{0010}\,\xi + a_{0001}\eta + \cdots \tag{2.41}$$

In a rotationally symmetric system, we can use a reduced version of this general expression for the wave polynomial. Denoting the wave aberration coefficients by W_{ijk}, where i, j, and k take integer values, we can write the aberration polynomial as [58]:

$$W_{ijk}\eta^i \rho^j (\cos\varphi)^k \tag{2.42}$$

2.8.3.1 Spherical aberration

The first of Seidels aberrations is spherical aberration, which can be expressed as [58]:

$$W(x,y) = W_{040}(x^2 + y^2)^2 = W_{040}\rho^4 \tag{2.43}$$

The source of this aberration is perfectly spherical lens radii. Such lenses are easier to manufacture, however, the outer parts of the lens are too strongly curved, therefore the rays from outer parts get focused closer than EFL of the lens. To eliminate these aberrations aspherical lenses should be used [57].

2.8.3.2 Coma

The second Seidels aberration is coma, which can be expressed as:

$$W(x,y) = W_{131}\eta(x^2 + y^2)y \tag{2.45}$$

and in rectangular coordinates [58]

$$W(x,y) = W_{131}\eta\rho^3 \cos\varphi \tag{2.46}$$

This type of aberration is seen when light comes from a point source at an angle with the optical axis. Due to lens imperfections the focal image resembles a comet rather than a dot [57].

2.8.3.3 Field curvature

The third Seidels aberration is field curvature, which can be expressed as:

$$W(x,y) = W_{220}\eta^2(x^2 + y^2) \tag{2.47}$$

and in rectangular coordinates

$$W(x,y) = W_{220}\eta^2\rho^2 \tag{2.48}$$

The field curvature has the same dependence on the pupil coordinates, x, y, or ρ, as defocus. Therefore, the two terms can be summed together in the following form [58]:

$$\begin{aligned} W(x,y) &= W_{220}\eta^2(x^2 + y^2) + W_D(x^2 + y^2) \\ &= (W_{220}\eta^2 + W_D)(x^2 + y^2) \end{aligned} \tag{2.47}$$

The field curvature can be treated both as point and field aberration, depending on if we look at is from a flat or curved field perspective [58]. As the name suggests field curvature is an aberration causing the focal points of a lens as obtained with different incidence angles not to lie on a plane, but rather on a curved surface [57].

2.8.3.4 Astigmatism

The fourth Seidels aberration is astigmatism can be expressed as [58]:

$$W(x,y) = W_{222}\eta^2 y^2 \tag{2.49}$$

Astigmatism causes rays propagating in two perpendicular planes to have different EFLs [61]. It causes the ideal circular airy pattern to blur into a diffuse circle, line, or elliptical shape, depending on the position of the focal plane [62]. Typically caused by optical elements having different lens curvatures for different axes. Due to it, there is no single point where all rays form a sharp focus [63]. A few of the possible ways to correct it are the use of spaced doublet lens with a stop in the center, cylindrical lens, or piezoelectric deformable mirrors [64].

2.8.3.5 Distortion

The final Seidels aberration is distortion, which can be expressed as:

$$W(x,y) = W_{311}\eta^3 y \tag{2.50}$$

Image distortions cause straight lines of an object to appear as curved in the resulting image. Common issues like barrel distortion and pincushion distortion often occur, especially when using wide-angle objectives [57] .

3. Experimental setup and methods

This thesis aims to evaluate the performance of various microlenses (ML) and microlens arrays (MLA) for relaying laser beams at varied distances within a multibeam nanolithography system. High transmittance, minimal optical aberrations, and high repeatability between individual beams are key factors for such a laser-based system.

Experimental tests were conducted to evaluate the optical parameters of custom-made and commercially available MLs. The evaluated optical properties included: reflection, transmission, and absorption coefficients, beam profiles, laser beam M^2 factor, and wavefront aberrations of different orders. These measurements required the design and assembly of specialized optical measurement systems.

3.1 Continuous wave laser system

During most of the experimental stages, optical setups were equipped with a LASOS LDM-XT series LD module, model VLD-XT 405120 (LASOS Lasertechnik GmbH. Franz-Loewen-Straße 2, 07745 Jena, Germany), as shown in Figure 3.1a. This LD has an average continuous-wave output power of 120 mW at a peak wavelength of 405 nm. The laser source is classified as Class 3B, which limits the maximum output power to 180 mW at 405 nm [65]. LD power could be adjusted between 1 - 100 % using LASOS laser control software. It is a free-space model with a Gaussian beam profile.

The beam was measured to have an average maximum output power of 127.69 mW, 6.4% higher than the specified datasheet power. For measurements where power level did not significantly affect result accuracy, the average power was set to the default value of 50%, corresponding to 63.86 mW.

Figure 3.1: Devices used for micro optics testing: (a) CW LD Lasos LDM-XT, with a max average output power of 120 mW, and center wavelength at 405 nm, (b) power meter Ophir Vega color laser power & energy meter, and 300 mW silicon photodiode Ophir PD300-UV.

For power measurements, an Ophir Vega color laser power and energy meter (Ophir Optronics. Science-based Industrial Park, Hartom St 6, Jerusalem, Israel) was used [66]. The energy meter was equipped with an Ophir PD300-UV photodiode capable of measuring up to 300 mW over a wide spectral range. Both the laser power meter (PM) and the photodiode are shown in Figure 3.1b. The photodiode came with a filter for higher power measurements and an aperture size of 10 × 10 mm. Made of UV-silicon and offers an ideal spectral range for our application of 200–1100 nm (220–1100 nm with the filter inserted). It has a maximum average power density of 10 W/cm² (50 W/cm² with the filter inserted) and a response time of 0.2 s [67].

Many of the measurement tools use complementary metal-oxide-semiconductor (CMOS) or charge-coupled device (CCD) sensors to capture the beam intensity profile or wavefront, and often the beam had to be focused onto the detector surface. ND filters were used in many setups to protect the pixels from excessive light flux. Some devices had in-built ND filters or motorized ND filter wheels, but for those that did not, we used a set of four ND filters with OD of 0.5, 1, 1.5, and 4, which could be used separately or in combination. A typical procedure would begin with the strongest ND filter of OD 1.5, and then, depending on the sensor's saturation level, we would either adjust the laser power between 1–100% or replace it with another ND filter.

3.1.1 Astigmatic beam

For beam intensity profiling, optical path alignment, aberration source identification, and other laser setup processes, the Edmund Optics Beam Profiler 4M (Edmund Optics. 101 East Gloucester Pike, Barrington, NJ 08007, USA) was used. This beam profiler, pictured in Figure 3.2a is equipped with a large area 11.3 x 11.3 mm CMOS sensor with a resolution of 2048 x 2048 at 5.5 μm pixel size, capable of 6.2 frame rate, when at full frame. The detector is rated for measurements of light sources with wavelength values between 350 – 1150 nm and a maximum average power of 1 W (CW saturation of 10 W/cm² at 1064 nm)

when equipped with an OD4 filter [68], which fits well with our 127.69 mW at 405 nm laser source.

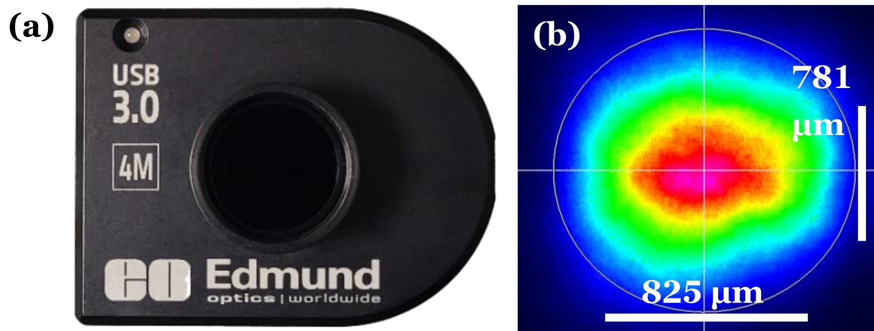

Figure 3.2: Astigmatism and beam ellipticity measurement and compensation setup. (a) Edmund Optics beam profiler 4M, with (b) beam profile measurement before SM fiber coupling.

Early on, we noticed that the beam produced by the LD was elliptical and diverged at different rates along the X and Y axes. This elliptical and astigmatic beam intensity profile can be seen in Figure 3.2b, showing measured beam diameter values at $1/e^2$ intensity. It is a typical feature of LDs to produce elliptical beams, however, for our application this was a critical issue to solve as for the most accurate ML aberration evaluation, we wanted a beam with an M^2 factor close to 1 (indicating a nearly perfect Gaussian beam) and an ellipticity close to 0 (meaning the beam profile is perfectly circular).

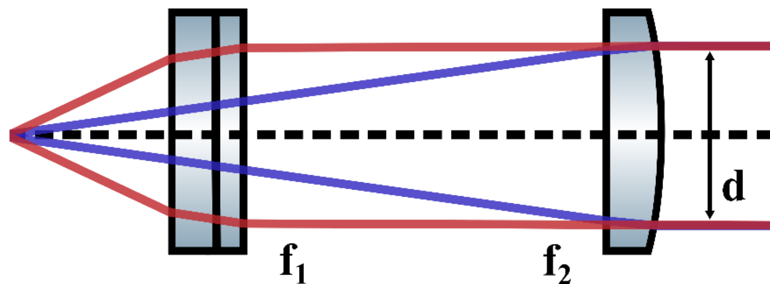

Figure 3.3: Schematic diagram of a beam expander using a pair of cylinder lenses with ELFs f_1 and f_2 used to match collimated beam diameters d in X and Y axes.

Our first solution involved placing two different EFL cylindrical lenses (EFL_x = 250 mm, EFL_y = 300 mm) orthogonal to each other, as shown in Figure 3.3. Each lens's focal point was positioned at the source of divergence to collimate the beam. However, to achieve a perfectly circular beam, this setup requires that the ratio of the cylindrical lenses' EFLs matches the ratio of the X and Y beam divergences [69].

After evaluating this setup, another issue became clear. As we were working with a small 825.5 × 781.5 µm beam, the beam was extremely sensitive to optical aberrations. Thus, even if the ellipticity and astigmatism were compensated for, the beam quality deteriorated.

3.1.2 Single-mode fiber coupling

Another solution to improve the astigmatic beam is to fiber-couple the LD. Coupling the beam into a SM fiber achieves spatial filtering by allowing only the fundamental transverse electromagnetic mode (TEM_{00}) to propagate efficiently, while higher-order modes or distortions such as astigmatism are filtered out. This results in a circularly symmetrical beam at the output, with an M^2 factor close to one. Fiber coupling is commonly available as a choice when buying a new LD. However, our model was old, and we did not have the choice to install a fiber coupler retroactively.

Therefore, we chose a pair of fiber couplers available in the laboratory. The astigmatic 825.5 × 781.5 µm beam was then coupled into a 125 ± 1.0 µm single-mode fiber with an FC/APC fiber connector with an 8° angled ferrule [70]. We used a TC25APC-405 FC/APC triplet collimator designed for a wavelength of 405 nm, with EFL of 24.77 mm and NA of 0.25 (Thorlabs Inc., 43 Sparta Ave, Newton, NJ 07860, USA) [71]. On the output side, we used another adjustable FC/APC fiber coupler designed for a wavelength of 405 nm. Based on the output beam diameter (measured at $1/e^2$) of $D_x = 2057.51$ µm and $D_y = 2051.76$ µm, the EFL is approximately 35.84 mm.

Typical coupling efficiency for elliptical 405 nm LDs ranges between 30 – 50 %, but in certain setups can be as high as 70 % [72]. To measure the coupling efficiency of our setup, the average power before P_L and after coupling P_F was measured as shown in Figure 3.4a, based on power levels set in the LASOS laser control software.

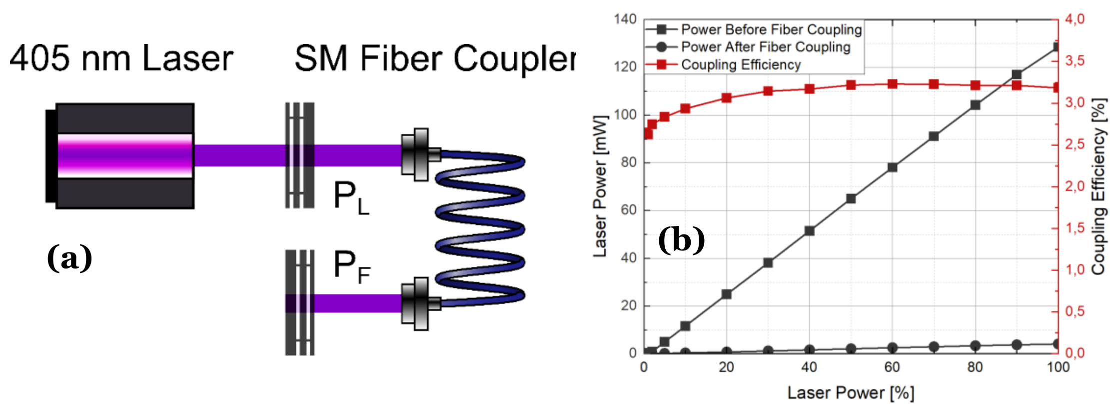

Figure 3.4: Fiber-coupled laser with coupling efficiency measurement setup and measured values. (a) Schematic of the coupling efficiency measurement setup. (b) Laser Coupling Efficiency Graph. Black squares represent the average direct laser power [mW] as a function of laser power level [%], while black circles show the average laser power after fiber coupling. The red line shows the coupling efficiency.

At higher laser power levels, the coupling efficiency stabilized around 3.13% (for more detailed results, see Figure 3.4b), which is a very low value. This could be explained by the limited XYZ and angular adjustment range on the input-side fiber

coupler and the high ellipticity of the first LD beam, resulting in much of the energy not coupling into the fiber. However, none of the further planned measurements were power-sensitive. Nonetheless, this significantly improved the laser beam quality, achieving an ellipticity of 0.01738 and M^2 factors averaging around 1.0704 × 1.0674.

3.2 Characterized microlenses

For evaluation, we chose a selection of custom-made and commercially available MLs and MLAs. A list of all the selected MLs with their respective parameters is given in Table 3.1. For multibeam nanolithography applications, the MLA pitch—and thus the lenslet diameter—was selected to be around 1 mm. While the EFLs of interest are larger than 50 mm, MLAs are typically designed for short EFL applications, such as wavefront sensors, light-emitting diode collimation, and imaging systems. Therefore, most off-the-shelf products did not have larger EFL counterparts. However, we wanted to evaluate what was available in the market, as these products were more affordable.

Table 3.1: Tested MLs with their respective parameters.

	MLA1	**MLA3**	**D200**	**D400**	**Meta Lens**	**F1I F1N**	**F2I F2N**	**F4I / F4N / GZPx**
EFL [mm]	5.3	14.6	200	400	100		200	400
Pitch [mm]	1x1.4	0.3	0.9	1.8	4	1.8		
Aperture	Rectangle	Square	Round					
Type	Refractive		Diffractive					
Material	PMMA	FS			Meta + FS	Cr + FS		
Coating	-	AR/AR (R < 1%)			-			
Array size	10x7	30x30	15x15		1	10x1		
Manufacturer	Thorlabs		Holo/Or		MOXTEK	Mycronic (custom thesis designs)		

To image the MLs and MLAs, we used a large-stroke CNC video measuring system, the Nikon Metrology NEXIV VMR-6555, as shown in Figure 3.5 (Nikon Metrology Inc., 12701 Grand River Ave, Brighton, MI 48116, USA) [73, 74]. This system is equipped with a large-area 650 × 550 mm stage, ideal for printed circuit board inspection, and two microscope objectives: a custom 6x objective and a Nikon LU Plan ELWD 50x/0.55 B EPI ∞/0 WD 9.8 objective. Additionally, the system has integrated optics providing an added magnification of 15x.

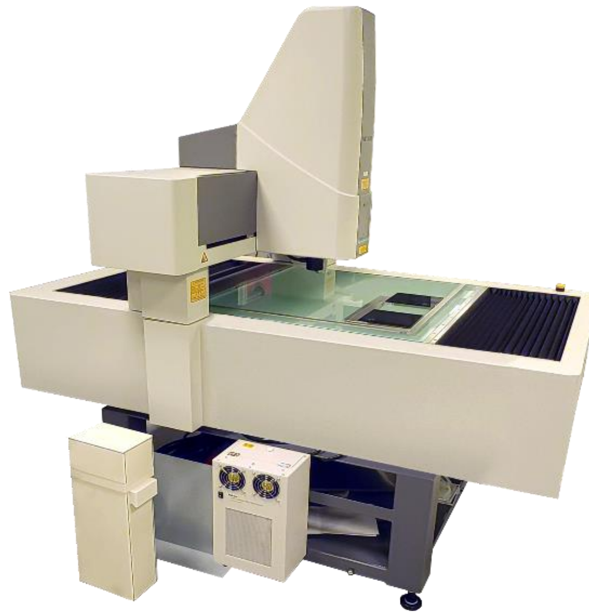

Figure 3.5: Nikon metrology NEXIV VMR-6555 large-stroke CNC video measuring system used for imaging MLs and MLAs.

3.2.1 Refractive lenses

Only two of the MLAs used were off-the-shelf products: MLA1M [75] (referred to as MLA1) and MLA300-14AR-M [76] (referred to as MLA3). Both are also the only refractive MLAs characterized during the project. We intended to include a GRIN lens for the characterization experiments, unfortunately we could not get hold of one due to delays in communication with suppliers and manufacturers.

MLA1 is a PMMA MLA, produced either by injection molding or hot embossing, which suggests that the surface quality may not be as high as lenses manufactured using other methods. The manufacturer specifies an EFL of 4.7 mm at 850 nm [75]. To determine the EFL at 405 nm, we used Ansys Zemax OpticStudio, an optical and laser system design, optimization, and simulation software (Ansys, Inc., 2600 Ansys Dr, Canonsburg, PA 15317, USA) [77]. Using the provided non-sequential mode Zemax model for MLA1 acquired on Thorlabs' website [75], we then calculated the EFL at 405 nm using the in-built merit function EFLX, which resulted in a value of 5.3 mm. Due to its very short EFL, MLA1 was expected to have significant spherical aberrations. Meanwhile, MLA3 is an FS MLA and is therefore expected to have better surface quality than MLA1.

3.2.2 Diffractive lenses

Additionally, to the refractive microlenses, we also characterized a range of diffractive MLs and MLAs. The diffractive MLs and MLAs tested were produced using various materials, fabrication methods, and diffractive patterns. These differences can affect their optical properties, which will be explored in the following sections.

3.2.3 Binary Fresnel zone plates

Additionally, to the refractive microlenses, we also characterized a range of diffractive MLs and MLAs. The diffractive MLs and MLAs tested were produced using various materials, fabrication methods, and diffractive patterns. These differences can affect their optical properties, which will be explored in the following sections.

Two different ZP pattern designs were fabricated in-house (Mycronic AB. Nytorpsvägen 9, 183 53 Täby, Sweden) [78]. The first design includes binary FZPs, designed for 405 nm wavelength, with lenslet pitch and lens diameter of 1800 µm, and three different EFLs of 100, 200, and 400 mm. Each EFL variant also had a negative pattern (appointed by 'N'), where the central zone was transparent rather than coated with Cr metal. While kinoform designs theoretically offer better suppression of higher-order beams, we were limited to a binary pattern fabrication due to the lithography technique used, which will be discussed in further chapters.

Examples of produced binary FZP patterns can be seen in Figure 3.6, and a full list of MLAs with their respective parameters available in Table 3.1.

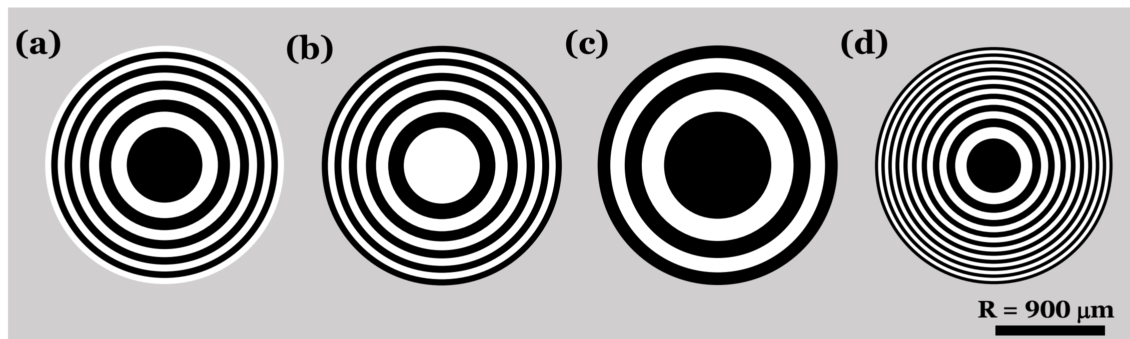

Figure 3.6: Fresnel zone plate designs, each with a 900 µm radius: (a) F2I and (b) F2N - designed with an EFL of 200 mm and an optimal zone period (n = 10) but inverted colors, (c) F4I - corresponding to double EFL of 400 mm (n = 5), and (d) F1I - featuring a reduced EFL of 100 mm with double the zone period (n = 20). Black zones correspond to Cr coating.

All the patterns were designed according to equations provided in Fresnel zone plates. The code was written in MATLAB platform (Mathworks. 1 Lakeside Campus Drive, Natick, MA 01760, USA) [79]. It allows for the adjustment of parameters such as wavelength, EFL, aperture radius, and inversion of the pattern. The generated pattern is exported in vector .svg format for more flexible adjustments in the later stages of fabrication.

Then the propagation trough FZP was simulated to highlight theoretical multi-order behavior of the diffracted beam. This was done using an adapted MATLAB script originally written by Ian Cooper (School of Physics, University of Sydney, Sydney, Australia) [80, 81]. The script allows to choose the wavelength, Fresnel zone count and EFL of the FZP. The adapted code could then calculate Fresnel zone radii and simulate laser beam propagation trough the FZP, calculating averaged irradiance values around the optical axis displaying EFLs of higher-order modes.

3.2.4 Gabor zone plates

Another set of ZPs fabricated in-house were GZPs. All GZPs were designed for 405 nm wavelength, with pitch and lens diameter of 1800 µm, EFL of 400 mm, and four different angular sector counts 11, 21, 42 and 84. Testing of patterns with different angular sector counts was purely out of curiosity.

Examples of produced GZP patterns can be seen in Figure 3.7, and a full list of MLAs with their respective parameters available in Table 3.1.

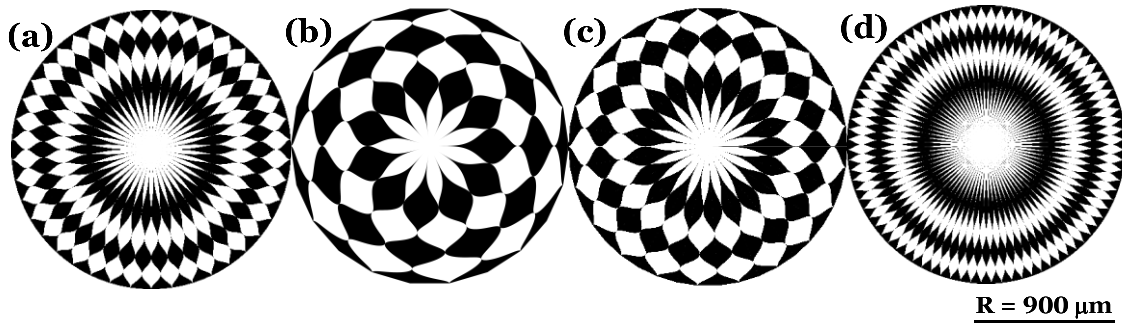

Figure 3.7: Gabor zone plate designs, each with a 900 µm radius: (a) GZP4 - designed with an optimal number ($N = 42$) of angular sectors, (b) GZP1 - corresponding to quarter ($N = 11$) the angular sectors, (c) GZP2 - corresponding to half ($N = 21$) the angular sectors, and (d) GZP8 - featuring a doubled number ($N = 84$) of angular sectors [82].

All the patterns were designed using an adapted MATLAB code, with the original GZP pattern generation code created by Vladimir Kesaev (Lebedev Physical Institute, Moscow, Russia) [82]. The code allows for the adjustment of parameters such as wavelength, EFL, aperture radius, and number of angular sectors. The generated pattern is exported in vector .svg format for more flexible adjustments in the later stages.

3.2.5 Kinoform Fresnel zone plates

Another set of diffractive lenses used were custom parameter kinoform-type FZPs from Holo/Or (Kiryat Weizmann High Tech Industrial Park, next to the Weizmann Institute of Science in Rehovot, Israel). D200 and D400 with their respective parameters available in Table 3.1.

3.2.6 Metalens

Another type of specialized diffractive lens used in this master's thesis project was a metalens provided by QuantumDesign (Quantum Design GmbH. Roddarestigen 3, 182 35 Danderyd, Sweden) [35] for this master's thesis and produced by Moxtek (MOXTEK, Inc., 452 W 1260 N, Orem, UT 84057, USA) [37]. This metalens is designed for 405 nm wavelength and features an aperture of 4 mm with an EFL of 100 mm. A protective overcoat is applied over the nanostructures to protect them from physical damage [35].

3.3 Zone plate manufacturing

The FZPs and GZPs discussed in the earlier section were fabricated in-house according to a custom design prepared during this thesis [78]. The final designs for two ZP arrays, each inside an aperture with a diameter of one inch (25.4 mm) were designed using KLayout layout editor (KLayout by Matthias Köfferlein), software intended for designing and inspecting integrated circuit designs. The final designs are shown in Figure 3.8, with detailed pattern data provided in Table 3.2.

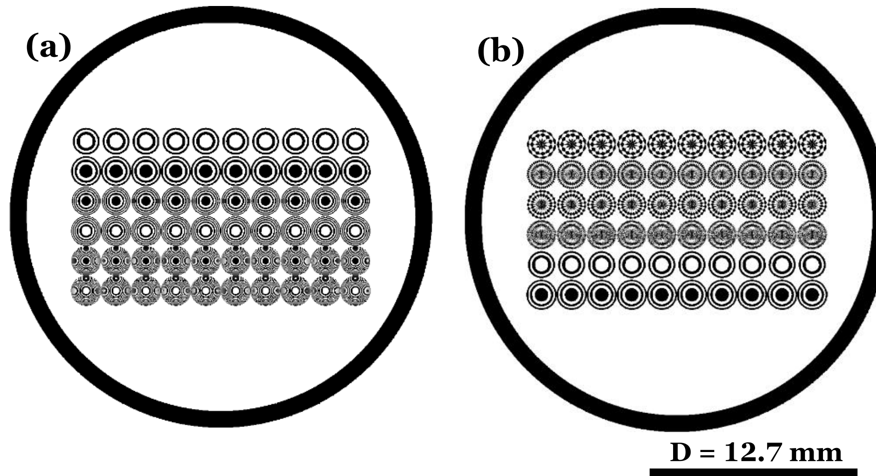

Figure 3.8: Final designs for two zone plate matrices, each with a diameter of 1 inch (25.4 mm). Both matrices have six different arrays of identical zone plates, repeated ten times. Each zone plate has a radius of 0.9 mm and a pitch of 1.8 mm. See Table 3.2 for exact parameters.

Table 3.2: Final design parameters for two zone plate patterns shown in Figure 3.8.

	Figure 3.8 - **Design (a)**						Figure 3.8 - **Design (b)**					
Row	1	2	3	4	5	6	1	2	3	4	5	6
Title Code	**F4I**	**F4N**	**F2N**	**F2I**	**F1N**	**F1I**	**GZP1**	**GZP4**	**GZP2**	**GZP8**	**F4I**	**F4N**
Array Size	10 x 1											
EFL [mm]	400		200		100		400					
Wavelength	405 nm											
Aperture radius	900 µm											
ZP Type	Fresnel						Gabor				Fresnel	
Inverse Pattern	✓	✗	✗	✓	✗	✓	✗	✗	✗	✗	✓	✗
Zone period	5	5	10	10	20	20	-				5	5
Angular period	-						11	42	21	84	-	

The prepared .svg vector data of the pattern was then converted into a format nano-lithographic mask writer could process. All the in-built compensations are applied to the pattern. A calibration writing is done right before to ensure the light is focused properly. Once all the settings are set, the plate can be printed. The plate is exposed with the pattern, and then processed in in-house processing machines. After patterning the plate was developed, dry-etched, and stripped. Finally, it was packaged and sent for water cutting.

3.4 Aperture filling

To ensure objective measurements of the ML performance, we aimed to fill the aperture as close to 100 % as possible using the available lenses in the laboratory, without overfilling it. We defined the beam width based on the $1/e^2$ intensity level (~13.5% of the peak value), therefore in most cases, we ended up underfilling the aperture. Overfilling could result in light leaking through adjacent lenslets, which potentially could lead to inaccurate measurement results.

3.4.1 Telescope

One of the solutions for aperture filling was using an adjustable 2.5x – 10x telescope designed for visible wavelength range. The telescope was placed after the fiber collimator and then placed in one of the two orientations either expanding or narrowing the beam width as needed. However, during testing multiple different problems became clear: the telescope was extremely sensitive to angular and linear adjustments, thus after each adjustment of magnification it would have to be realigned. Also, adjusting the magnification not only affected the beamwidth but also the M^2 factor and introduced aberrations to the beam. At 2.5x magnification the beam maintained a slightly worse M^2 value of 1.090 x 1.169, but at maximum magnification, the beam quality deteriorated significantly, making it unsuitable for characterizing microlenses, with M^2 values of 1.259 x 1.322.

3.4.2 Lens matching

The chosen solution for aperture filling involved placing a matched lens with a combined EFL beside the characterized ML, while aiming to fill as much of the ML aperture as possible. To find suitable matching lenses for each characterized ML, we defined the beam to have a collimated diameter of 2057.64 μm at a wavelength of 405 nm. Using Zemax OpticStudio's sequential mode and the merit function RAID, we optimized the spacing between the two lenses to collimate the beam, while the REAY merit function allowed us to optimize for the desired final beam width. This process led to Table 3.3, which includes a complete list of all characterized MLs and MLAs with their respective matched lenses. When a suitable lens could not be found, we selected a lens with a lower aperture fill.

Table 3.3: Matched lenses according to selected MLs.

ML	**MLA1**	**MLA3**	**D200**	**D400**	**Meta**	**F1x**	**F2x**	**F4x / GZPx**
EFL [mm]	5.3	14.6	200	400	100		200	400
Pitch [mm]	1 x 1.4	0.3	0.9	1.8	4	1.8		
Matched Lens	**L1560**	**P51.5**	**P257.5**		**P30.9**	**L1986**	**L1484**	**P257.5**
EFL [mm]	24.9	100	500		60	124.6	299	500
Magnification	0.213	0.146	0.4	0.8	1.667	0.803	0.669	0.8
Aperture fill [%]	43.8	100.1	91.45		85.74	91.74	76.46	91.45

3.5 Light interaction with microlenses

Light transmittance is a crucial parameter in nano-lithography setups. Since lithography is sensitive to light flux and optical setup includes many optical elements, accounting for optical losses is important. Therefore, we went ahead to evaluate the light interaction parameters of our measured microlenses, including transmission, reflection, and absorption coefficients. In both setups, the measured absorption values also include scattered light components. To obtain exact average power readings, we used two different setups with a free-space laser beam. The laser beam quality should not affect the accuracy of the results. The free-space laser beam width was measured to be 830.5 x 775.5 µm. For evaluations, we used were 1-inch (2.54 cm) broadband dielectric mirror, designed for the 400–750 nm range, which has a reflectance value of approximately 99.9% at 405 nm [83].

3.5.1 Small angle power measurement setup

The first setup for evaluating light interaction parameters involves placing the ML or MLA at a small angle θ_i from perpendicular to the incoming laser beam (90° - θ_i) as shown in Figure 3.9. For curved refractive MLAs reflection and back-scattering coefficients are expected to be higher as the incoming beam is angled with the optical axis of the MLs.

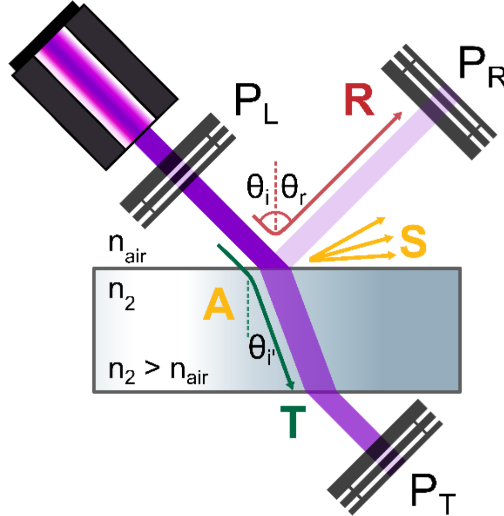

Figure 3.9: Small-angle power measurement setup for evaluating ML light interaction parameters.

In our setup $\theta_i = \theta_r = 2.53°$. Then four power measurements are taken: P_{Ref} – reference background value, P_L – direct laser power, P_R – power reflected from the surface of the element, and P_T – power transmitted through the optical element. These average power values allow us to estimate light interaction parameters according to the following equations:

$$T = \frac{P_T - P_{Ref}}{P_L - P_{Ref}} \tag{3.1}$$

$$R = \frac{P_R - P_{Ref}}{P_L - P_{Ref}} \tag{3.2}$$

$$A + S_B = 1 - T - R \tag{3.3}$$

where T – transmission, R – reflection, and $A + S_B$ – sum of absorption and back-scattered light coefficients. Due to setup and available measurement tool limitations, the absorption and back-scattered light is kept as a single coefficient.

3.5.2 Beam splitter power measurement setup

Another setup for evaluating light interaction parameters involves placing a BS at 45° angle with the laser beam. This setup allows for measurements of ML reflections when the incoming beam is perpendicular to the ML surface. The model of the BS used in the setup is the WW41050 UVFS wedge window. This BS features a 1-inch (2.54 cm) diameter aperture with 5mm thickness, 30 ± 10 arcmin wedge angle, and is designed for 185 – 2100 nm wavelength range, with a transmission coefficient of approximately 93 % at 405 nm [84]. The setup layout is shown in Figure 3.10.

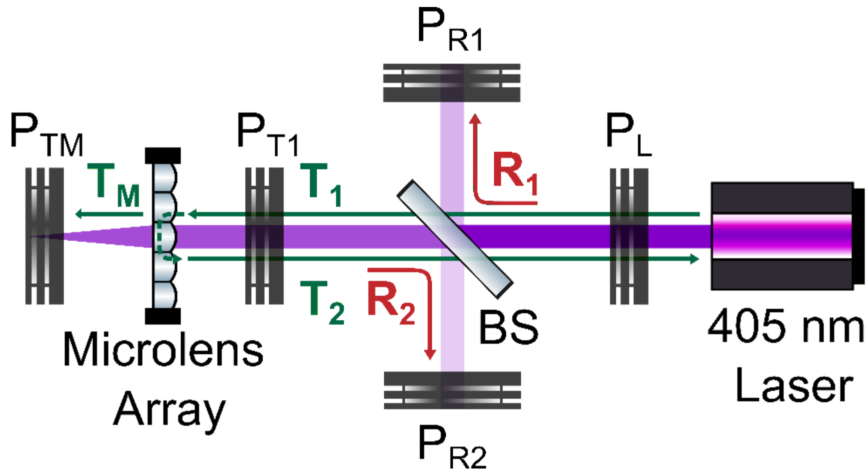

Figure 3.10: Beam splitter power measurement setup for evaluating beam splitter and ML light interaction parameters.

Six power measurements are taken: P_{Ref} – reference background value, P_L – direct laser power, P_{R1} – power reflected from the outer air-glass and inner glass-air interface surfaces of the BS, P_{T1} – power transmitted through the BS, P_{TM} - power transmitter through the ML, and P_{R2} – power of light traveling backwards, reflected from both the outer air-glass and inner glass-air interface surfaces of the BS. These average power values allow us to estimate light interaction parameters for BS (appointed by '1') according to the following equations:

$$T_1 = \frac{P_{T1} - P_{Ref}}{P_L - P_{Ref}} \tag{3.4}$$

$$R_1 = \frac{P_{R1} - P_{Ref}}{P_L - P_{Ref}} \tag{3.5}$$

$$A_1 + S_{B_1} = 1 - T_1 - R_1 \tag{3.6}$$

and light interaction parameters for ML (appointed by 'M') according to the following equations:

$$T_M = \frac{P_{TM} - P_{Ref}}{P_{T1} - P_{Ref}} \tag{3.7}$$

since,

$$R_1 = R_2 \tag{3.8}$$

$$R_2 = \frac{P_{R2} - P_{Ref}}{P_{T2} - P_{Ref}} \tag{3.9}$$

therefore,

$$P_{T2} = \frac{P_{R2} - P_{Ref}}{R_2} + P_{Ref} = \frac{P_{R2} - P_{Ref}}{R_1} + P_{Ref} \tag{3.10}$$

and

$$R_M = \frac{P_{T2} - P_{Ref}}{P_{T1} - P_{Ref}} = \frac{P_{R2} - P_{Ref}}{R_1(P_{T1} - P_{Ref})} \tag{3.11}$$

$$A_M + S_{B_M} = 1 - T_M - R_M \tag{3.12}$$

3.6 M^2 factor measurement setup

One of the methods to evaluate the beam quality is to measure M^2 factor of the beam. For this task, we used an Ophir Spiricon M²-200s laser beam analyzer, seen in Figure 3.11a, equipped with a 1600 x 1200 CCD sensor, 7.5 Hz frame rate, and a 4.4 µm pixel size. Figure 3.11b displays internal schematic of the device featuring a fixed focusing lens with EFL of 330 mm and a 161.19 mm travel distance motorized Z-stage.

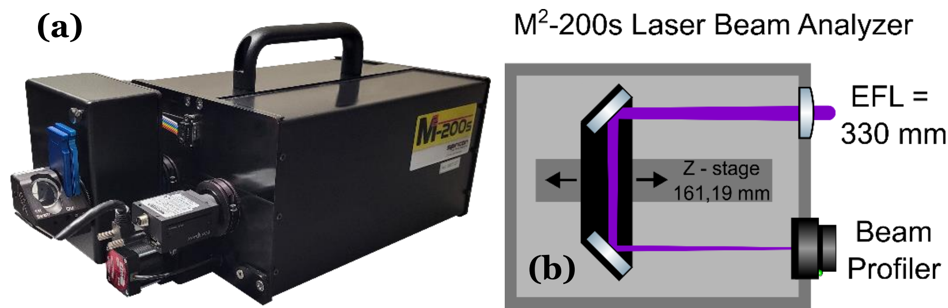

Figure 3.11: Laser beam analyzer used for M^2 factor measurements: (a) Ophir Spiricon M^2-200s laser beam analyzer, and (b) schematic illustrating the internal workings.

Figure 3.11b displays internal schematic of the device featuring a fixed focusing lens with EFL of 330 mm and a 161.19 mm travel distance motorized Z-stage. This lens focuses collimated or low divergence beam onto the beam profilers' CCD sensor. To avoid overexposure, the device uses a motorized OD filter ring, which adjusts automatically based on how strongly the beam is focused.

The beam profiler correlates beam width with different Z-stage values for both X and Y axes. This allows for a device to calculate beam parameters for X and Y axes such as beam width, waist width, divergence, waist location, M^2 factor, BPP, Rayleigh range, and combined values such as astigmatism and asymmetry of the beam.

3.6.1 Laser reference

To evaluate the M^2 factor of the fiber coupled laser (FCL), we aligned the beam with the optical rail and guided the beam directly into the laser beam analyzer with a pair of perpendicular mirrors (BB1-E02) as seen in Figure 3.12.

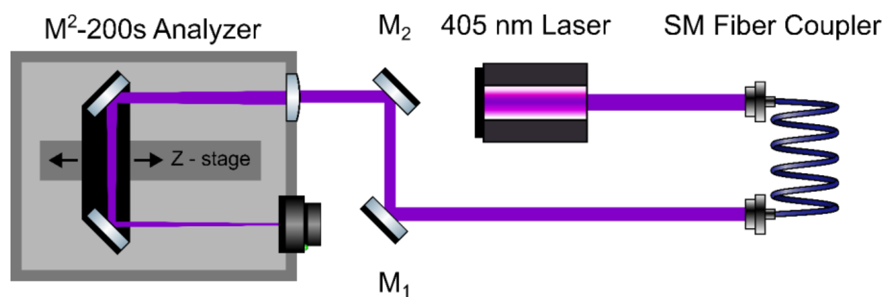

Figure 3.12: Setup for evaluating the M^2 value of the SM-coupled laser beam. The beam is directly guided into the laser beam analyzer using a pair of mirrors.

3.6.2 Focusing lens characterization

To evaluate the M^2 factor of the matched lenses described in Table 3.3, we used a pair of identical lenses placed at a distance equal to double their EFL apart.

This setup focuses and re-collimates the beam back to its original beamwidth, as seen in Figure 3.13.

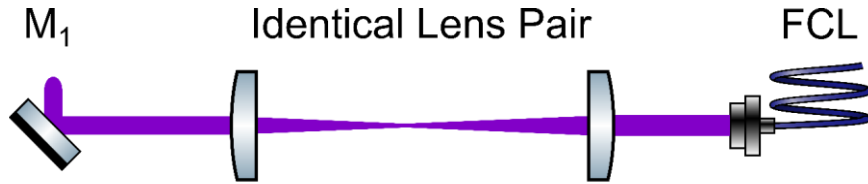

Figure 3.13: Setup for evaluating the M^2 value of a selected lens. A pair of identical lenses are positioned at twice the EFL distance from each other to focus and re-collimate the laser beam.

By comparing the measured M^2 factor of the beam after it passes through the two matched lenses with the laser's reference M^2 value, we can evaluate the contribution of a single lens to the overall M^2 factor. To evaluate the M^2_{Lens} of a single lens we apply the following equation:

$$M^2_{lens} = \sqrt{\frac{M^2_{Lens\,pair}}{M^2_{Laser\,reference}}} \tag{3.13}$$

where $M^2_{Lens\,pair}$ is the measured M^2 factor of the identical lens pair, and $M^2_{Laser\,reference}$ is the M^2 factor of directly measured LD beam.

3.6.3 Microlens characterization

To evaluate the M^2 factor of the MLs and MLAs described in Table 3.1, we used sets of MLAs along with their matched lenses, as described in Table 3.3. Then we placed the two lenses at a distance equal to the sum of their EFLs. This setup focuses and re-collimates the beam before re-entering the M^2 laser beam analyzer, as shown in Figure 3.13.

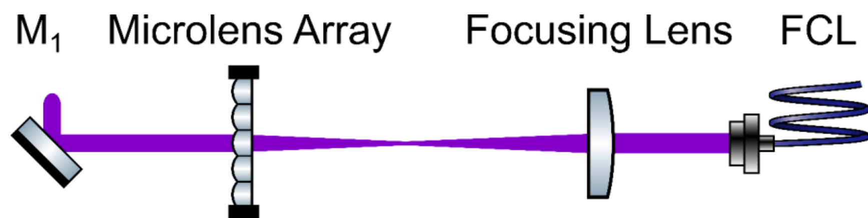

Figure 3.14: Setup for evaluating M^2 values of an ML. A characterized matching lens is used to focus light and fill the ML aperture while re-collimating the light.

Multiple measurements were recorded for each lenslet in the MLA, to evaluate variance of the M^2 factor between the lenslets. By comparing the measured M^2 factor of the beam after it passes through a combination of a ML and its matched lens with the laser's reference M^2 factor (and accounting for the known M^2 factor contributions introduced by the matched lens) we can evaluate the M^2

factor contributions introduced by the ML itself. Therefore the M_{ML}^2 for the MLs can be evaluated through the following equation:

$$M_{ML}^2 = \frac{\frac{M_{Lens+ML}^2}{M_{Laser\ reference}^2}}{M_{Lens}^2} \tag{3.14}$$

where $M_{Lens+ML}^2$ is the measured M^2 factor of the ML with a matched focusing lens.

3.7 Wavefront measurement setup

To evaluate the exact types of aberration introduced by the MLs and MLAs we used a Shack–Hartmann wavefront sensor (SHWFS) Optocraft SHSCam – HR3-130-GE-PRO UV (Optocraft GmbH., Am Weichselgarten 7, 91058 Erlangen, Germany) shown in Figure 3.15a [85]. This SHWFS is equipped with an 8.4 x 7 mm a wavefront sensor designed for wavelength range between 266 – 405 nm, with lateral resolution of 63 x 53, with greyscales at 12 bit, and 24 Hz frame rate [86].

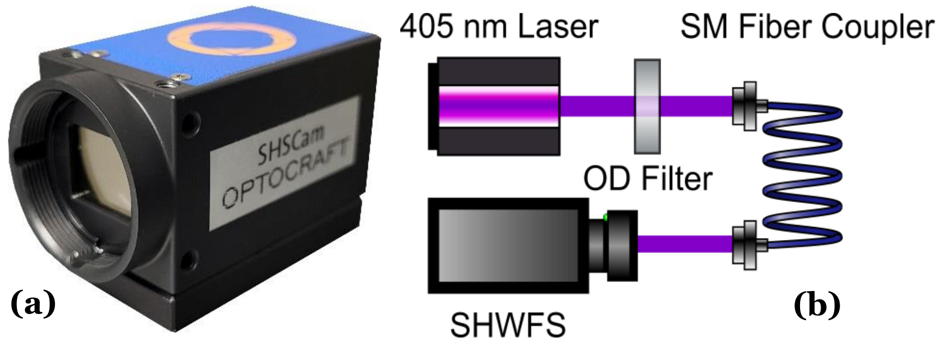

Figure 3.15: Setup to measure the reference laser wavefront: (a) utilizing a Shack-Hartmann wavefront sensor, Optocraft SHSCam – HR3-130-GE-PRO UV, and (b) schematic showcasing the SM-coupled laser beam wavefront being directly measured.

In the software interface for SHWFS called SHSWorks (Optocraft GmbH., Am Weichselgarten 7, 91058 Erlangen, Germany), firstly a calibration file for 405 nm wavelength measurements is applied. A successful measurement gives a broad list of measured optical parameters such as general sum Zernike coefficient, wavefront tilt angle, beam width and position on the sensor, M^2 value, beam waist position, Rayleigh range, Zernike amplitude coefficients (C_0 – C_{15}) and more. As well as a power density profile, SHWFS also rebuilds the wavefront of the incoming beam, and calculates the corrected (spherical to flat) wavefront.

Zernike amplitude coefficients stand for the magnitude of specific aberrations according to Equation 2.38. In the SHWFS setup used, each coefficient corresponds to a distinct type of aberration: C_0 – piston aberration, C_1 – wavefront tilt along the X-axis, C_2 – wavefront tilt along the Y-axis, C_3 – defocus aberration, C_4 – 1st order astigmatism at 0°, C_5 – 1st order astigmatism at 45°, C_6 – coma along the X-axis, C_7 – coma along the Y-axis, C_8 – spherical aberration.

3.7.1 Laser reference

To evaluate the wavefront aberrations, present in FCL beam, we aligned it with the optical rail and guided the beam directly into the SHWFS as shown in Figure 3.15b. An OD filter in combination with laser power control is used to reduce the flux of the laser beam to protect SHWFS from damage. This measured wavefront is used as a laser reference for further evaluation of MLs and MLAs aberration contributions.

3.7.2 Focusing lens characterization

To evaluate the aberrations introduced by the matched lenses described in Table 3.3, we used a pair of identical lenses placed at a distance equal to double their EFL apart. This setup focuses and re-collimates the beam back to its original beamwidth, as seen in Figure 3.16.

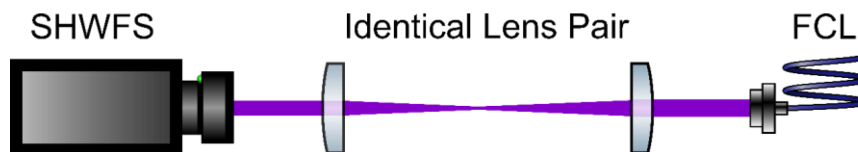

Figure 3.16: Setup for measuring selected lens wavefront. A pair of identical lenses are positioned at twice the EFL distance from each other to focus and re-collimate the laser beam.

By comparing the measured wavefront of the beam after it passes through the two matched lenses with the laser's reference wavefront, we can evaluate the aberrations introduced by a single lens.

3.7.3 Microlens characterization

To evaluate the aberrations introduced by the MLs and MLAs described in Table 3.1, we used sets of MLAs along with their matched lenses, as described in Table 3.3. Then we placed the two lenses at a distance equal to the sum of their EFLs. This setup focuses and re-collimates the beam before re-entering the SHWFS, as seen in Figure 3.17.

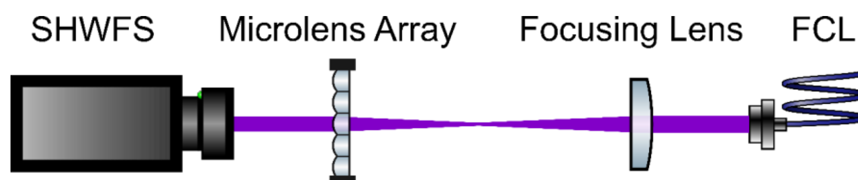

Figure 3.17: Setup for measuring wavefronts of the ML. A characterized matching lens is used to focus light and fill the ML aperture while re-collimating the light. The two lenses are positioned at the combined EFL of both lenses.

Multiple measurements were recorded for each MLA, to evaluate variance of the wavefront aberrations between the lenslets. By comparing the measured wavefront of the beam after it passes through a combination of a ML and its matched lens with the laser's reference wavefront (and accounting for aberrations introduced by the lens) we can evaluate the aberrations introduced by the ML itself.

4. Results

The results of the conducted experiments described in the section Experimental setup and methods done are summarized in this section.

4.1 Laser diode properties

The first LD beam profile showed high ellipticity and strong astigmatism. This is an inherent edge-emitting LD characteristic, as the active cross-sectional area is typically rectangular, with the width and height of the emitter varying significantly. This results in different beam divergence angles of the parallel (θ_{slow}) and perpendicular (θ_{fast}) orientations.

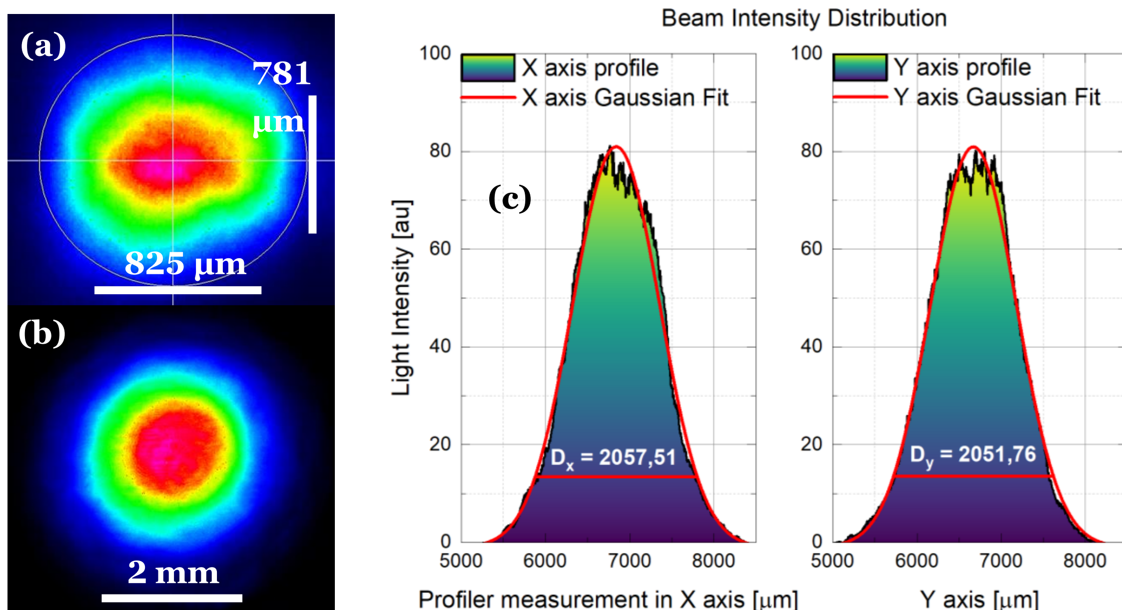

Figure 4.1: Beam profile measurements: (a) Beam profile before SM fiber coupling (beam diameters D_x = 825 ± 5.5 µm, D_y = 781 ± 5.5 µm), (b) beam profile after SM fiber coupling (beam diameters D_x = 2057 ± 5.5 µm and D_y = 2051.5 ± 5.5 µm), (c) beam intensity profiles along the X and Y axes with Gaussian fits.

Using an M^2 beam analyzer, the initial beam indicated relatively low M^2 factor values of M_x^2 = 1.072 ± 0.0005 and M_y^2 = 1.143 ± 0.0005, with X-axis value corresponding to the θ_{fast} and Y to the θ_{slow}. θ_{fast} = 1.147 mrad, and θ_{slow} = 1.086 mrad. The astigmatism was measured to be 0.42 ± 0.005. Beam intensity distribution was measured using a beam profiler.

The beam showed strong ellipticity as shown in Figure 4.1a, with beam diameters D_x = 825 ± 5.5 µm and D_y = 781 ± 5.5 µm. According to Equation 2.26, this large variation in beam diameters in two perpendicular axes corresponds to an ellipticity of 0.0533 ± 0.0032.

As a first solution, we used a pair of cylindrical lenses, as shown in Figure 3.3, with EFL_x = 250 mm and EFL_y = 300 mm. This setup compensated for the inherent LD astigmatism, reducing it to 0 ± 0.005. However, because the pair of cylindrical lenses were not perfectly matched to the relative divergence angles θ_{slow} and θ_{fast}, the resulting beam remained elliptical, with an ellipticity coefficient of 0.0498 ± 0.0029. Additionally, new aberrations were introduced by the lenses, as the M^2 factor reduced down to M_x^2 = 1.117 ± 0.0005 and M_y^2 = 1.258 ± 0.0005.

4.2 Single-mode fiber coupling

For clearer interpretation of the ML and MLA measurement results, we prefer to have the reference LD beam M^2 shows a Gaussian intensity profile, which would result in M^2 factor equal to 1.

By coupling the beam into SM fiber, we eliminate the higher-order spatial modes and allow only the fundamental mode to propagate, this leads to a near-perfect Gaussian-like beam intensity profile, as shown in Figure 4.1b.

Using the measured beam profile intensity data from the beam profiler, where the diameter is fitted according to a Gaussian distribution, we obtain diameter values of D_x = 2057 ± 5.5 µm and D_y = 2051.5 ± 5.5 µm, as shown in Figure 4.1c. This corresponds to beam ellipticity of 0.01738 ± 0.0003 according to Equation 2.26. Since an ellipticity of zero shows a perfect circle and one stands for a line, our resulting beam is almost perfectly circular.

The astigmatism for the SM fiber-coupled LD was reduced to 0.02 ± 0.005. Although this value did not match the performance achieved using the pair of cylindrical lenses, it is still a significant improvement over the initial beam.

4.3 Characterized microlenses

Using the acquired Gaussian-like beam, we then went ahead with the characterization of all the several types of MLs and MLAs listed in Table 2.1. All the micro-optics were imaged under a microscope at 6x magnification, as shown in

Figure 4.2. This inspection allowed us to check the micro-optics for any surface defects that might cause added optical aberrations.

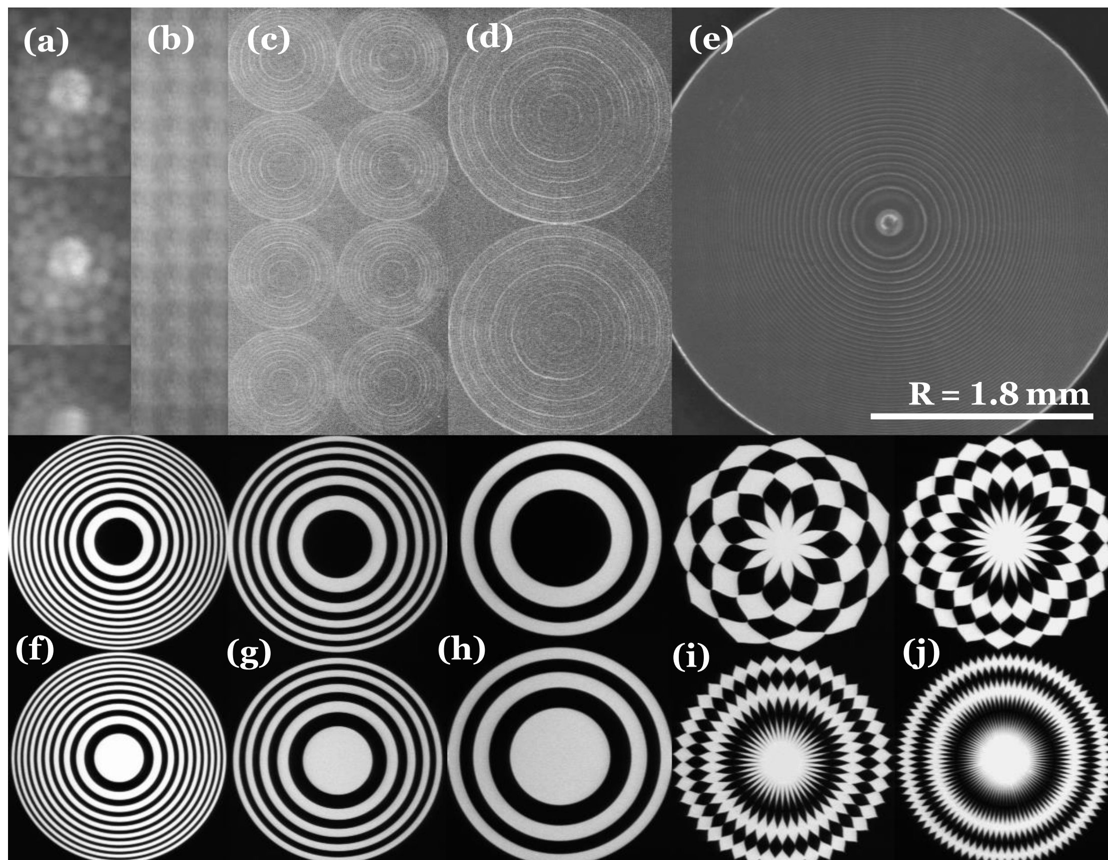

Figure 4.2: Pictures of characterized lenses under Nikon NEXIV VMR-6555 microscope with 6x magnification. All pictures are to scale with each other. Parameters of each lens can be found in Table 3.1, with broader information about FZPs and GZPs in Table 3.2. Displayed lenses: (a) MLA1, (b) MLA3, (c) D200, (d) D400, (e) Meta, (f) F1I and F1N, (g) F2I and F2N, (h) F4I and F4N, (i) GZP1 and GZP4, and (j) GZP2 and GZP8.

The list includes a wide range of micro-optics. As the two MLAs (MLA1 and MLA3) are refractive, capturing clear images was rather difficult. The two DOEs (D200 and D400) clearly displayed the diffractive structure within the FS substrate.

Ten differently patterned zone plates were produced in-house, consisting of three initial design FZPs (F1I, F2I, and F4I), three negative pattern FZPs (F1N, F2N, and F4N), and four GZPs (GZP1, GZP2, GZP4, and GZP8). All of them showed no deviations from their original designs.

During the first observation, an odd asymmetrical formation in the central zone of the metalens stood out, as seen in Figure 4.2e. Therefore, we imaged the micro-optics using higher magnification objectives, with a magnification factor of 50x.

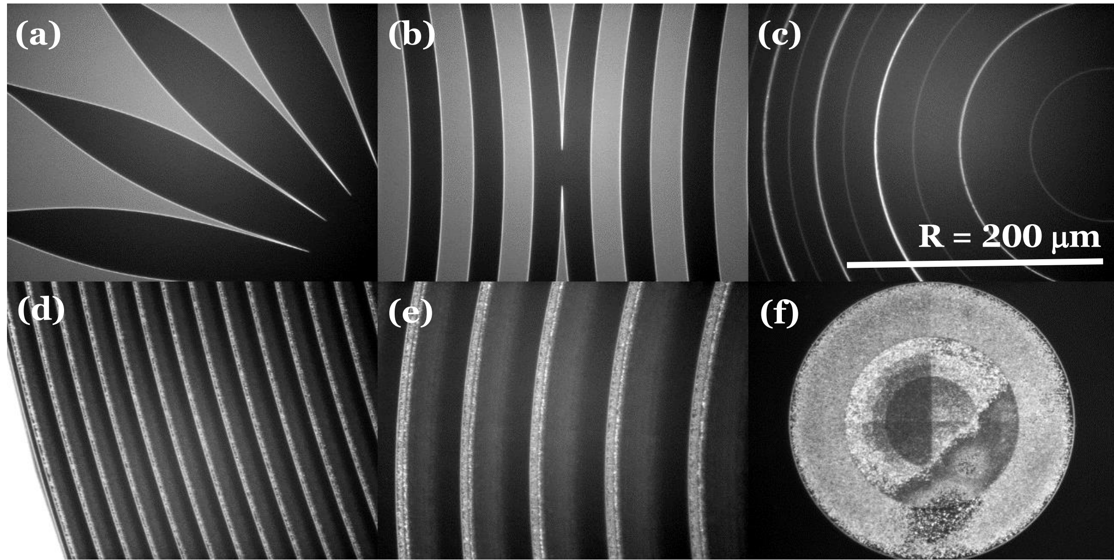

Figure 4.3: Pictures of characterized lenses under Nikon NEXIV VMR-6555 microscope with 50x magnification. All pictures are to scale with each other. Displayed lenses: (a) GZP2 side profile, (b) two parallel F4Is pattern contact, (c) D200, (d-f) metalens outer rings profile, middle rings, and central part observation.

In Figure 4.3a, a close-up of the GZP2 angular sectors can be seen, along with the two F4I patterns contact in Figure 4.3b. Figure 4.3c provides a clearer view of the circular zones within the DOE substrate material. Figure 4.3d and Figure 4.3e showcase the geometry of the metalens, resembling the continuous kinoform profile discussed in the Background section, Suppressing higher-order modes.

Lastly, the previously mentioned asymmetry in the central zone of the metalens is shown in Figure 4.3f. Due to the un-symmetric nature of this formation, it is likely to be a result of either mechanical or laser flux-induced damage to the structure of the metalens.

Since this formation was only observed after all experimental measurements were carried out, it is difficult to determine whether the damage was present upon delivery of the metalens or occurred during testing. Given that the formation is quite small (around 80 μm) relative to the 4 mm diameter of the metalens aperture, it is not expected to significantly impact the final results of the measurements discussed later.

4.4 Light interaction with microlenses

To evaluate lens performance in an optical system, it is crucial to account for optical losses by evaluating light-matter interaction parameters, such as transmission, reflectance, absorption, and backscattered light coefficients.

4.4.1 Small angle power measurements

The first setup, described in Experimental setup and methods section, Small

angle power measurement setup, involves placing the optics of interest at a small angle, which in our case was $\theta_i = \theta_r = 2.53°$. The light transmitted through the lens and reflected from its surface was measured using a laser power meter. The evaluated reflectance, transmission, absorption, and backscattered light coefficients are displayed in Figure 4.4.

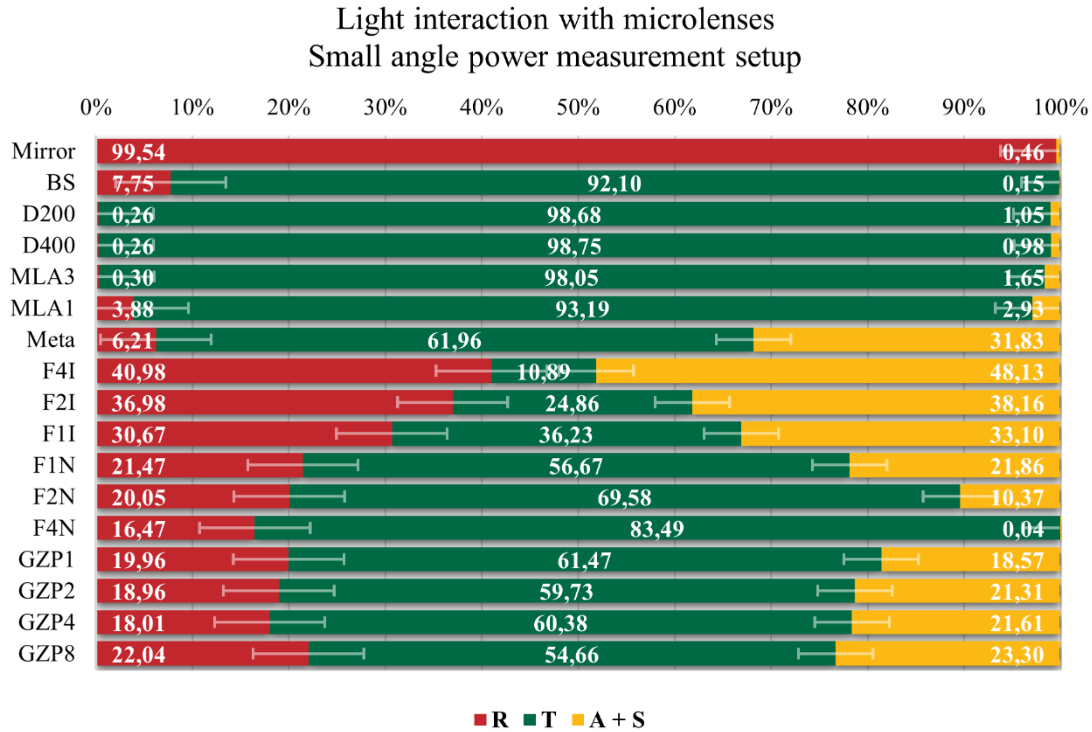

Figure 4.4: Evaluated reflectivity, transmission, and absorption + back-scattered light coefficients (% values) for selected optics from small angle power measurements. For expanded results, refer to the Figure A in Appendix.

As expected, a reference measurement using a broadband mirror showed an extremely high reflectance of 99.54 %, with no measurable transmittance. The reflectance stated by the manufacturer is 99.77195 % at a 405 nm wavelength [83]. The wedge BS, used in the following section, showed a reflectance of 7.75 %, with the manufacturer's reflectance value listed as 6.9699 % ($T = 93.0301$ % and $R = 1 - T$) at 405 nm [84].

The DOE lenses showed the lowest optical losses of all the tested micro-optics, allowing over 98.5% of light to pass through. This was unsurprising, given that they were coated with anti-reflective coatings on both sides of the substrate, and the FS material itself has excellent transmittance. The same applied to MLA3, which also had anti-reflective coatings on both sides of the MLs and was made of FS glass.

MLA1 performed worse, likely due to its uncoated surface nature and the fact that PMMA absorbs more light at shorter wavelengths closer to the UV range.

The metalens reflected a small part of light, with a transmittance of 61.96 %. A significant amount of light was lost due to absorption and backscattering. Since these losses were relatively high, we checked the surface temperature of the metalens using a thermal camera during maximum power exposure. The lens did not show strong heating effects, leading to the conclusion that majority of the losses from coefficients $A + S_B$ were due to backscattering. This makes sense, as the complex 3D kinoform-like geometry of the lens likely caused substantial light scattering. This aligns with the theory that metalenses tend to show higher losses, one of their known disadvantages [33].

The in-house fabricated FZPs showed the highest reflectance coefficients for the initial design patterns. This is because these lenses had large, reflective Cr-coated central zones that acted as small-scale mirrors, with F4I, having the largest central zones, reflecting the most light.

The opposite was true for the negative patterns, where F4N, with the largest transparent central zone, transmitted the greatest part of light. The negative pattern variants also showed the lowest losses, leading to the highest transmission coefficients. While we lacked the equipment to measure backscattered light, it was visibly clear using a laser viewing card.

The in-house GZPs showed similar light-matter interaction behavior, as the ratio of Cr-coated to transparent regions remained constant, with the only difference being the number of angular sectors. The slightly larger absorption and backscatter coefficients for GZP8 could be attributed to the increased number of small-scale structures, which scattered more light, while the variations in reflectance coefficients were within the margin of error.

In general, for both FZPs and GZPs, the reflectance coefficients appeared to be directly dependent on the ratio of Cr-coated to transparent regions for the laser beam distribution on the surface of the lens.

For the metalens, FZPs, and GZPs, additional data is available in Appendix section A.2.1 Expanded small angle power measurement results These expanded results include an additional set of measurements where the metalens, FZPs, and GZPs were positioned with either the pattern facing the laser source first (XXX-P) or with the glass substrate facing the laser source (XXX-G).

4.4.2 Beam splitter power measurements

Another set of light-matter interaction measurements was carried out using a BS-based setup, as described in the Experimental setup and methods section, Beam splitter power measurement setup. The advantage of this setup is that it allows for direct, perpendicular measurement of lens surface reflection and transmission, unlike the small-angle setup, where a small angle must be introduced to enable power measurements. The measurement results are presented in Figure 4.5.

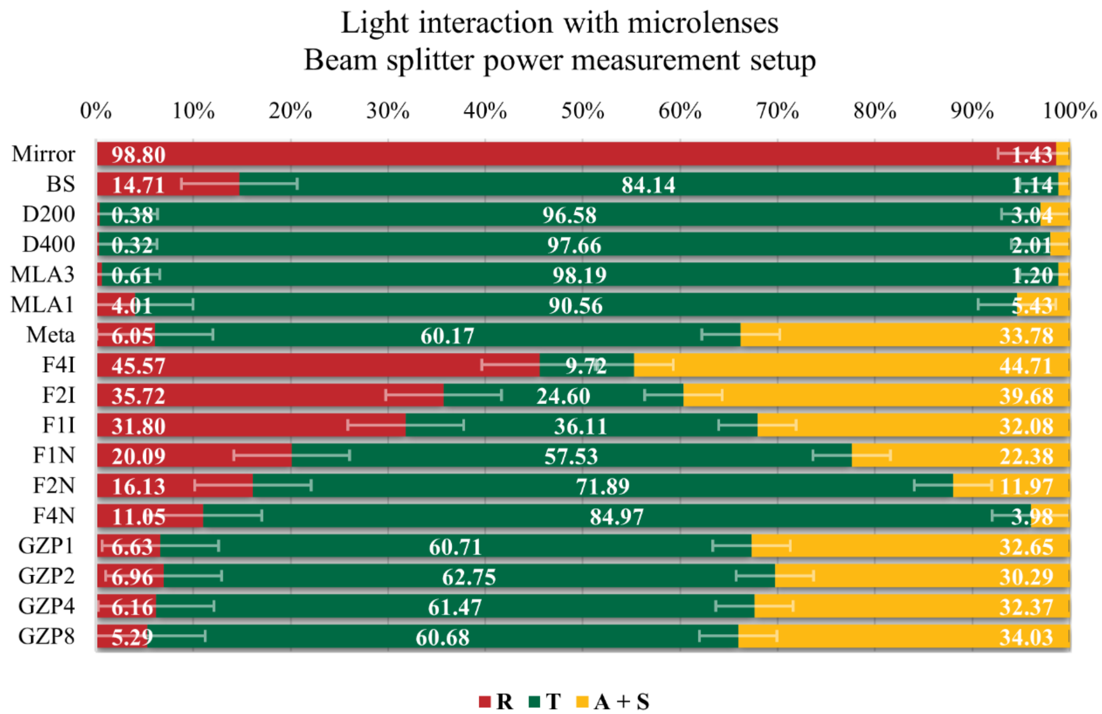

Figure 4.5: Evaluated reflectivity, transmission, and absorption + back-scattered light coefficients (% values) for selected optics from beam splitter power measurements. For expanded results, refer to the Figure A in Appendix.

In terms of optics positioning, the BS in this setup was placed at a 45° angle, rather than a small angle (θ_i), which is clear from the results, as the reflection coefficient is nearly double that of the small-angle setup.

For the metalens, FZPs, and GZPs, an additional set of data is available in Appendix section, titled A.2.2 Expanded beam splitter power measurement results These expanded results include additional measurements where the metalens, FZPs, and GZPs were placed with either the pattern facing the laser source first (XXX-P), or with the glass substrate facing the laser source (XXX-G).

4.4.3 Results comparison

For a better comparison of the results, the values from both the small-angle power measurement setup and the BS-based power measurement setup were plotted on a single bar chart, as shown in Figure 4.6.

Most of the results align well with each other, except for the BS values, which differ due to the varied orientation between the two measurements. The higher reflectivity values for the GZPs in the small-angle setup could be explained by increased absorption and backscattering in the BS setup. The part of light reflected in the small-angle setup was transferred to the absorption and backscattering coefficient in the BS setup, while transmission remained relatively similar.

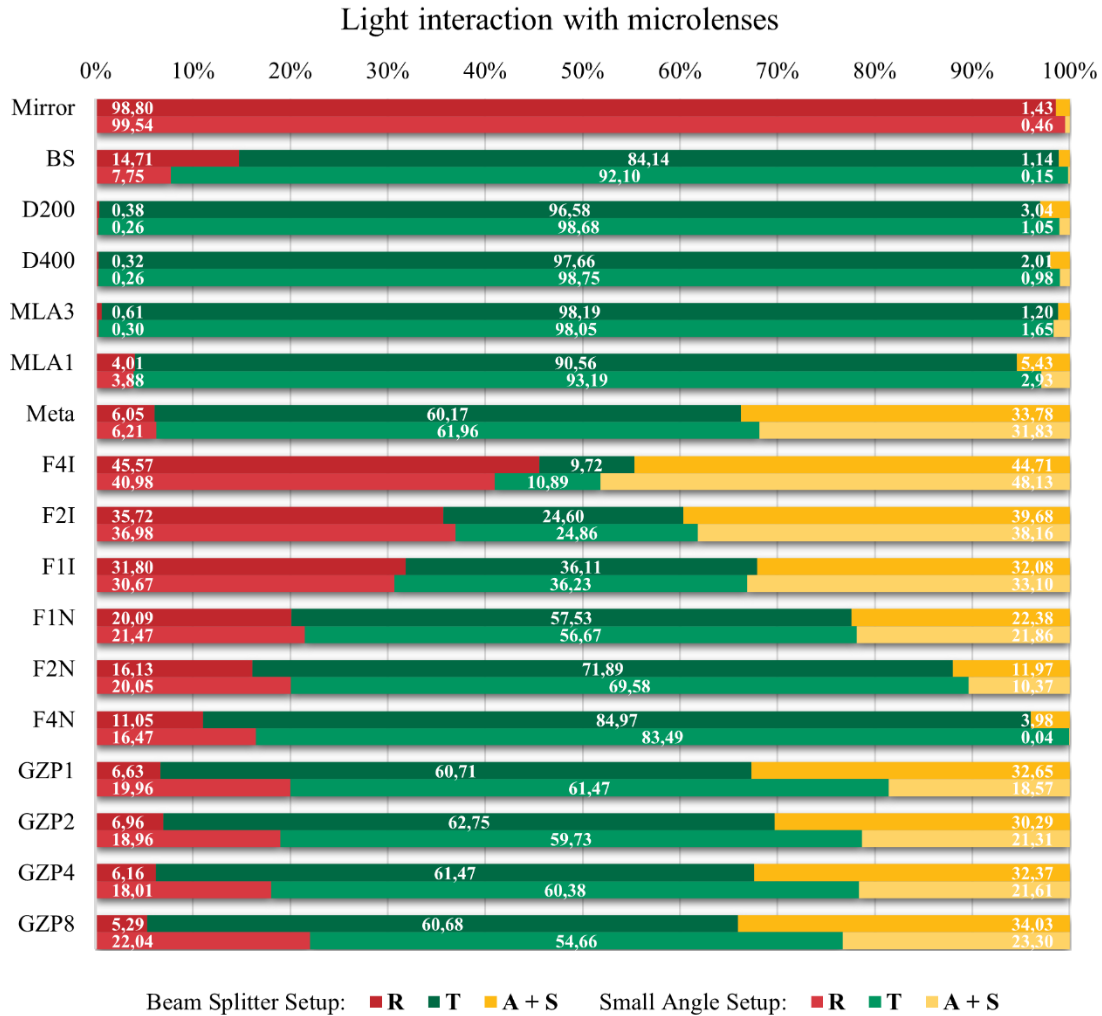

Figure 4.6: Evaluated reflectivity, transmission, and absorption + back-scattering coefficients for selected optics. Clustered results with beam splitter setup results above, and small angle setup values below. For expanded results, refer to the Figure A in Appendix.

4.5 Beam propagation

Diffractive optics inherently involve higher-order modes, which are typically unwanted and must be suppressed. Binary FZPs lack higher-order mode suppression mechanisms, unlike the GZPs, metalens, or DOEs that were tested. To show multi-modal beam behavior, beam propagation simulations were conducted for the tested FZPs, with all the simulated and experimental results presented in Figure 4.7.

As shown in Figure 4.7a, the F4N lens with a 400 mm EFL, in the simulation of axial intensity distribution along the optical axis, exhibits higher-order focal lengths at distances f, f/3, f/5, f/7, etc., according to Equation 2.10. Additionally, the beam intensity distribution at the first-order EFL in the plane orthogonal to the optical axis was simulated and is shown in Figure 4.7b-c. This distribution illustrates what one should expect to see at the EFL of the given FZP. To confirm the simulation results, a measurement was performed using an M^2 beam analyzer,

with the resulting image displayed in Figure 4.7d. Comparing simulated Figure 4.7b and the measured Figure 4.7d, a clear resemblance can be observed, validating the simulation results.

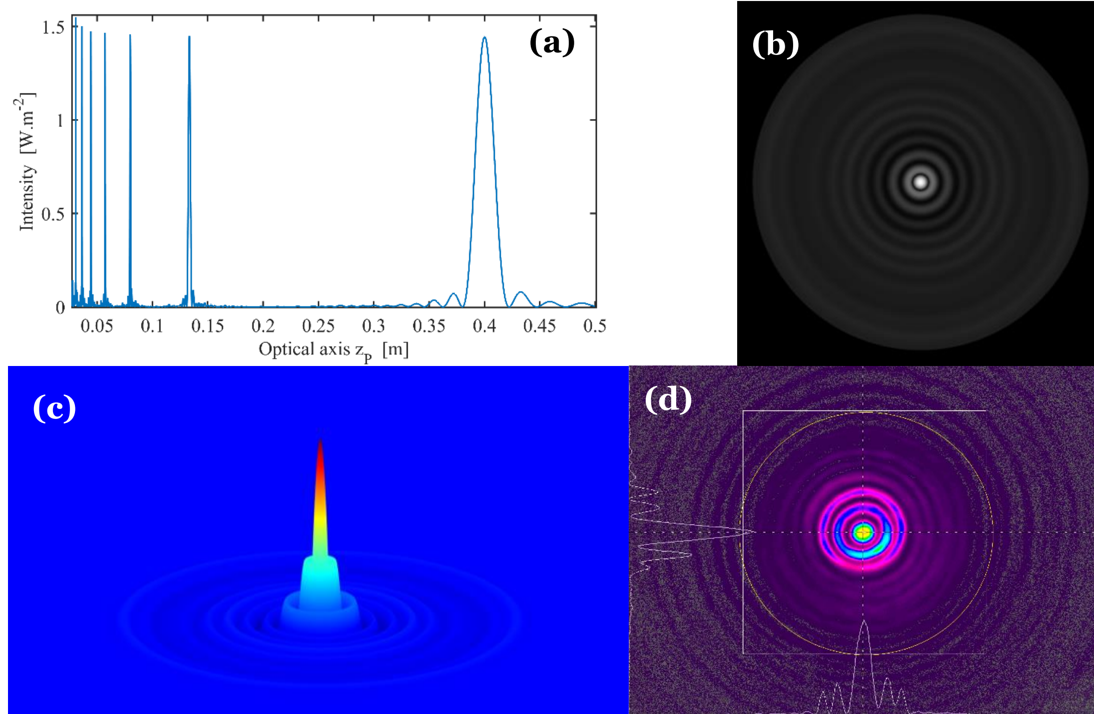

Figure 4.7: Multi-order behavior of the F4N lens with a 400 mm EFL. Simulated (a) axial intensity distribution along the optical axis, and (b-c) simulated beam intensity distribution at the first-order EFL of 400 mm in the orthogonal plane to the optical axis. Experimental validation (d) displaying multi-order behavior of the F4N lens using M^2 beam analyzer.

To show the beam propagation of the GZPs and their ability to suppress higher-order modes, beam intensity distribution measurements were conducted. Defocus measurements (150 mm away from the EFL) are shown in the top part of Figure 4.8, and measurements at the EFL are displayed in the bottom part for all the fabricated GZPs (GZP1, GZP2, GZP4, and GZP8).

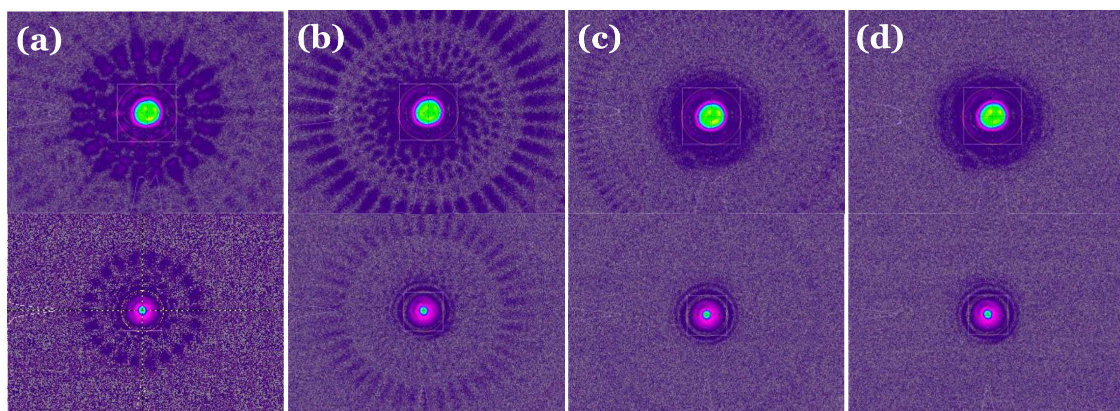

Figure 4.8: Multi-order behavior of the GZPs. Defocus (150 mm from EFL) beam intensity distribution on top, and at EFL in the bottom. Including all the fabricated GZPs in increasing angular sector count from left to right with (a) GZP1, (b) GZP2, (c) GZP4, and (d) GZP8.

Even at defocus, the GZPs with a higher number of angular sectors were much more effective at suppressing higher-order modes. For the GZP with an EFL of 400 mm, a 1.8 mm diameter, and a wavelength of 405 nm, the best number of angular sectors was 42, corresponding to the GZ4 pattern. Given this ideal number of 42, we can also observe that it was the first pattern to fully suppress higher-order modes at the EFL distance. The same applies to the GZ8 pattern, which has 84 angular sectors.

4.6 M² factor measurements

The first M^2 factor measurement using the M² beam analyzer was conducted to find the reference value for the SM fiber-coupled LD. The methods for M² factor analysis are described in the Experimental setup and methods section, M² factor measurement setup. The reference M^2 factor measurement is shown in Figure 4.9, with (a) displaying the beam profile at the EFL distance, and (b) illustrating the beam spot size dependence on the Z-stage distance, along with the measured beam parameters on the right-hand side.

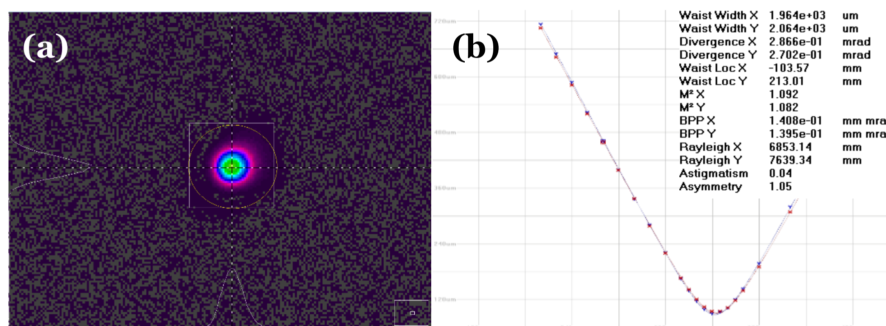

Figure 4.9: Laser reference M² factor measurement: (a) the beam profile, (b) the beam spot size dependence on the Z stage distance. X-axis M² = 1.092, Y-axis M² = 1.082, astigmatism at 0.04.

The average M^2 factor value for the LD source is M_x^2 = 1.077 ± 0.0005 and M_y^2 = 1.086 ± 0.0005. Following this, all M^2 factors for focusing lenses were evaluated, with measurement results provided in Appendix section A.2.4 M² factor measurements for focusing lenses. Subsequently, the M^2 factors for the characterized MLs and MLAs were evaluated, with the results shown in

Many measurements were conducted, making this the most time-consuming part of the thesis, as each individual measurement took ~10-15 minutes. For the MLAs, an average of 15 measurements were made to evaluate the repeatability between lenslets.

During the testing of FZPs and GZPs, an aperture was introduced after the zone plates in a few measurements to spatially filter higher-order modes. The averaged values showed the best M^2 factor, even improving the FCL beam quality, showing the usefulness of spatial filtering in certain optical setups.

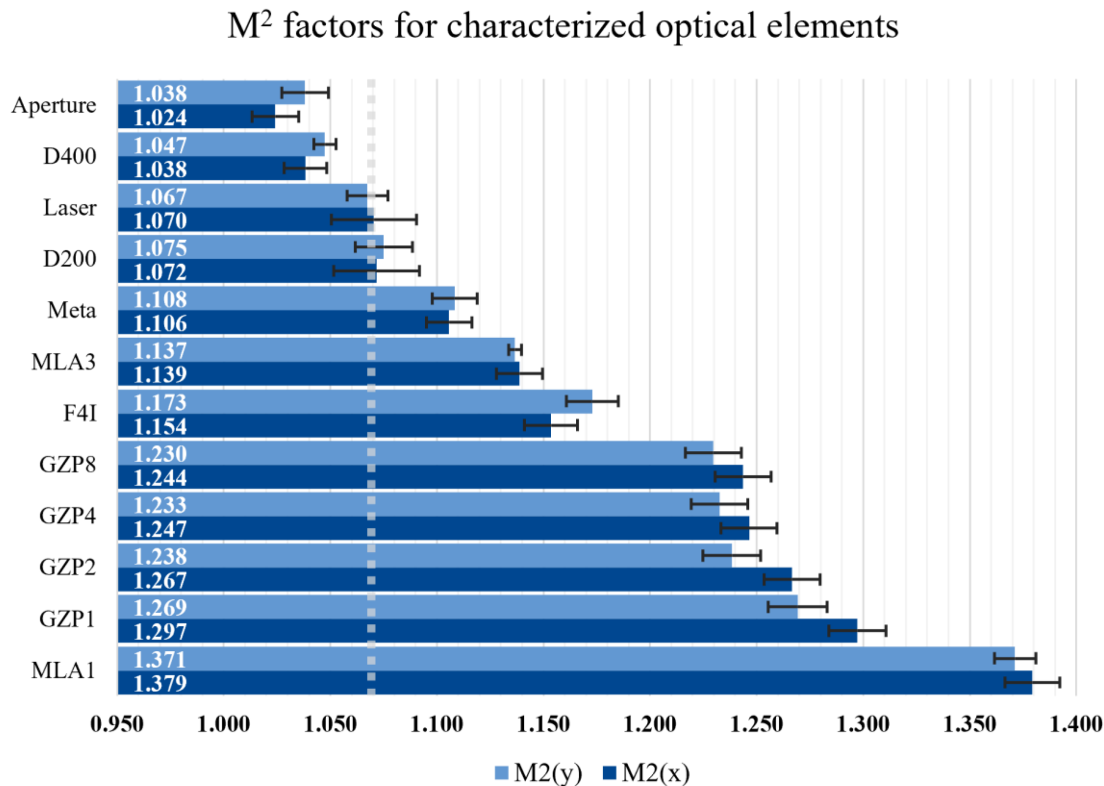

Figure 4.10: M^2 factors for characterized optical elements. The dashed line stands for the average M^2 factor of 1.069 for the LD source.

The best M^2 factors were shown by the two DOEs, D200 and D400. Both lenses had insignificant effect on beam quality, and surprisingly, D400 even slightly improved it. This consistent result suggests that the kinoform DOEs may suppress optical aberrations inherent to the SM fiber-coupled beam, or that new aberrations introduced by the DOE coincidentally canceled out those inherent to the FCL, improving beam quality.

The metalens exhibited excellent M^2 factor values, aided by its relatively large 4 mm aperture. It effectively suppressed higher-order modes, although the impact of the asymmetric formation observed in the Characterized microlenses section is assumed to be minimal due to its small size relative to the aperture.

MLA3 performed even better, likely due to the small aperture size of the MLs. With a pitch of just 300 µm, MLA3 is sensitive to surface quality. The high quality of the FS glass surface led to low optical aberrations and, so, a low M^2 factor.

M^2 factor values for the FZPs could not be accurately evaluated because the M^2 beam analyzer lacks a feature to eliminate higher-order modes, which had high peak intensities. Only a single successful measurement was made for F4I, likely due to its large transparent central zone, allowing most light to pass through and focus at the EFL with minimal higher-order modes.

GZPs were the second worst-performing MLs. As expected, the best M^2 factor was achieved with GZP4 and GZP8, which had the largest angular sector counts. This confirmed that, as predicted by theory, 42 angular sectors are optimal, as increasing beyond this point did not significantly improve beam quality.

As expected, the worst-performing MLA was MLA1. During the optical design phase in Zemax, it was clear that these lenses will show strong spherical aberrations if the aperture fill factor approached 100%. Additionally, MLA1's rectangular aperture limited aperture filling according to the width of the shorter side. Microscopic inspection also revealed non-perfect surface quality on the PMMA lens, with visible scratches and distortions.

All measured MLs showed highly consistent results between measurements. Similarly, MLAs showed consistent M^2 factor repeatability across different lenslets in the array, with variations within the range of measurement error.

4.7 Wavefront measurements

Another method to evaluate the optical performance of an ML or MLA is by measuring the optical aberrations it introduces. This can be done by assessing how an optical element distorts the wavefront, which can be measured using SHWFS. The SHWFS can evaluate several parameters for the incoming wavefront, including the general sum of Zernike polynomial term root mean square (RMS) value, as well as individual Zernike amplitude coefficients for specific Zernike polynomial terms (C_0 – C_{15}). An example SHWFS measurement for defocused FCL is shown in Figure 4.11.

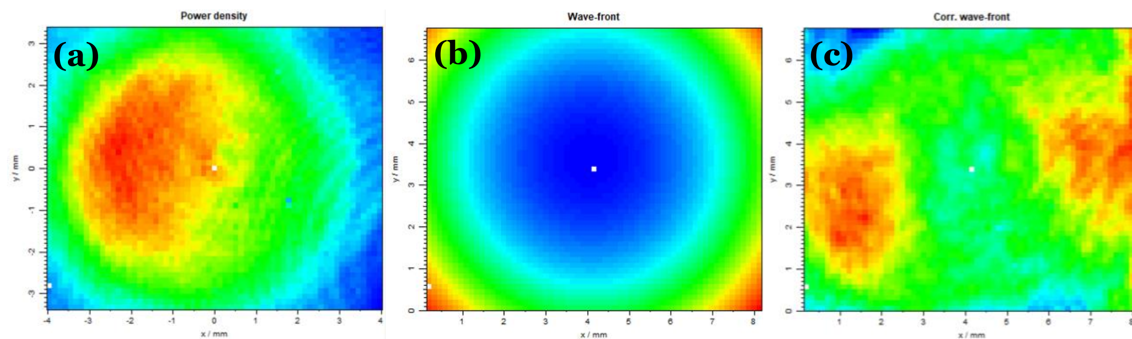

Figure 4.11: The SHWFS wavefront measurement for an FCL beam defocused using a concave lens, with the measured beam intensity profile on the left, the actual measured wavefront in the middle, and the corrected wavefront on the right, highlighting the aberrations inherent to the beam.

First, a reference FCL wavefront measurement was recorded, followed by evaluating the aberrations introduced by the focusing lenses. Then, a series of measurements were conducted for all the MLs and MLAs of interest. After subtracting the focusing lens term, we were able to isolate and evaluate the aberrations introduced by the MLs and MLAs, with the results shown in Figure 4.12.

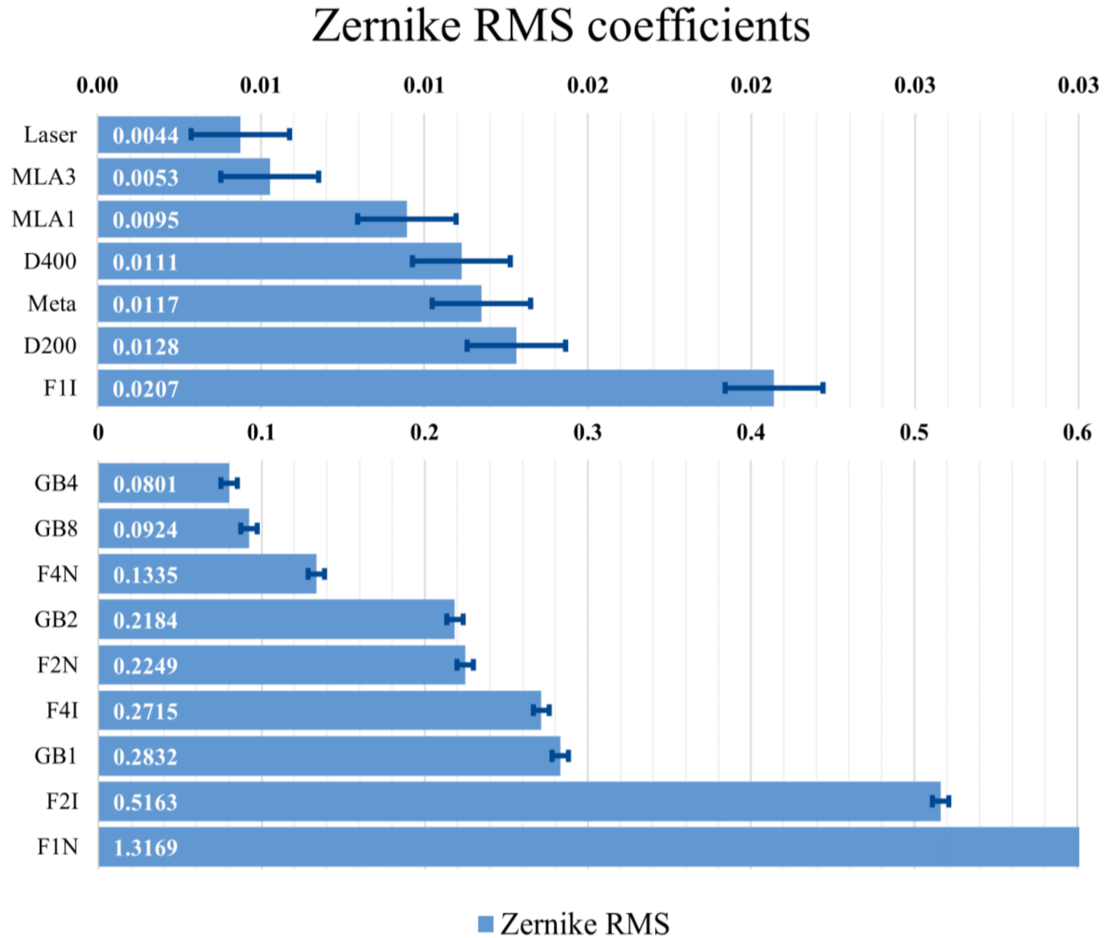

Figure 4.12: General combined Zernike root mean square (RMS) term for the different measured lenses.

A table showcasing the general Zernike terms, as well as the specific Zernike polynomial terms (C_0 – C_{15}), for the MLs and MLAs measurements, can be found in Appendix section A.2.5 Wavefront measurements. Terms C_0 – C_2 primarily show optical alignment effects, with C_0 standing for overall phase shift (piston), and C_1 – C_2 indicating wavefront tilt. C_3 stands for the flatness of the wavefront. The lower-order aberrations (C_4 – C_8) are the most interesting, as they relate to optical performance. However, these terms are quite small for the best-performing micro-optics. As a result, the general Zernike coefficient becomes more significant in evaluating overall performance.

The laser source showed the lowest Zernike polynomial value, showing that all the other lenses introduced some aberrations to the wavefront. The Zernike RMS term of 0.0044 shows a high-quality beam with minimal wavefront aberrations.

The best results were seen with both refractive MLAs (MLA1 and MLA3). This makes sense, given that these lenses are less sensitive to alignment errors. MLA3 performed significantly better than MLA1, likely due to superior surface quality achieved during FS MLA fabrication. Additionally, FS is more resistant to scratching and other mechanical effects.

Both DOEs and the metalens performed similarly, within the error range. This time, the metalens outperformed the D200, although the trend from the M2 factor measurements still holds, where D400 performed better than D200. The similar performance of these three diffractive lenses highlights the current state of the art, as all are designed to suppress higher-order modes and share similar aperture sizes and EFL distances. As a result, the choice of lens often depends on the specific implementation and budget.

The strongest aberrations were introduced by the zone plates. FZPs performed poorly due to the lack of a higher-order mode suppression mechanism. GZPs performed slightly better, once again showing that a higher number of angular sectors improves beam quality. This time, GZP4 introduced fewer aberrations than GZP8.

5. Discussion

This thesis aimed to evaluate various ML and MLA technologies for applications in multi-beam nano-lithography systems. We tried to evaluate their optical losses and ability to maintain high beam quality. This discussion focuses on an analysis of the experimental results, how well they compare to the literature, and possible applications of these results in the field of nano-lithography.

5.1 Refractive micro-optics

Refractive microlenses are still the go-to option in optical systems due to their simplicity. In this thesis, several refractive microlens arrays (MLAs) were characterized for their ability to collimate laser beams. The results show that while refractive microlenses can achieve effective beam collimation, their performance is limited by optical aberrations.

The M^2 factor measurements showed that refractive microlenses introduced optical aberrations, which reduced the beam quality. This finding is consistent with the literature, as refractive microlenses are known to suffer from such limitations, especially when the EFL is short and surface quality is not ideal.

While the tested refractive microlenses may not be ideal for high-precision applications without additional corrections, they still hold potential in multi-beam systems when using better-quality customized MLs and MLAs.

5.2 Diffractive micro-optics

The diffractive optics tested in this thesis provided an interesting comparison to traditional refractive optics. Diffractive optics focus light by changing its phase rather than its direction. This approach provides several advantages, by reducing the physical thickness of the optical elements while maintaining similar focal lengths and allowing for highly custom designs with various beam shaping, and compensation mechanisms. During this thesis, binary FZPs and GZPs were fabricated and evaluated.

The experimental results have shown that binary FZPs suffer from multi-order diffraction effects. As predicted by theory and simulations, binary FZPs create multiple focal points along the optical axis. These additional focal points introduce unwanted interference patterns which result in worse beam quality. This multi-order behavior was observed experimentally, showcasing higher-order foci around first-order mode at EFL distance.

To compensate for the multi-order behavior, GZPs were tested. They use a radial variation in the zone structure to focus light into a single focal point, effectively suppressing the multi-order behavior observed in binary FZPs. The suppression of higher-order modes was shown to be effective, with minimal higher-order modes present, especially when using the optical count of angular sectors. This makes GZPs useful in applications, where maintaining small focus is critical. The ability to customize and fabricate binary GZPs using standard lithographic techniques makes them an appealing option.

Another method to suppress higher-order modes is to use DOEs or metalenses. The results showed that such MLs maintained the best beam quality in comparison to all the other types of MLs. According to the literature DOEs have been shown to achieve better beam quality in micro-optics applications. However, while more customizable, DOEs and metalenses involve relatively complex fabrication steps, making them less cost-effective.

One of the main limiting factors for the accuracy of the results was the alignment of the laser with the MLs, as even small misalignments could result in significant deviations in beam quality. This was particularly true both for the M^2 factor measurements and SHWFS measurements.

This thesis provides a detailed comparison of multiple microlens technologies under the same measurement conditions. DOEs offer a promising optical solution for beam guiding in nano-lithography systems. Their ability to suppress higher-order modes and maintain great beam quality makes them fit for high-precision applications.

6. Conclusions

During this thesis, a wide variety of MLs and MLAs were tested. The list included both refractive and diffractive micro-optics of different shapes, sizes, and patterns.

After coupling the LD beam into an SM fiber, we improved the beam quality from M_x^2 = 1.092 ± 0.0005 and M_y^2 = 1.143 ± 0.0005 to M_x^2 = 1.077 ± 0.0005 and M_y^2 = 1.086 ± 0.0005. Additionally, astigmatism was reduced from 0.42 ± 0.005 to a low value of 0.02 ± 0.005, and the ellipticity of the beam improved from 0.0533 ± 0.0032 to 0.01738 ± 0.0003.

Before further evaluation, all MLs and MLAs were inspected under a high-magnification microscope. MLA1 showed slight surface imperfections, and the metalens had an unsymmetrical formation in its central zone, which could have negatively impacted beam quality if that formation was unintended. All the in-house fabricated FZPs and GZPs perfectly matched their intended design patterns, with no noticeable surface quality issues.

All the micro-optics were characterized based on light-matter interaction parameters, such as transmittance, reflectance, absorption, and scattering coefficients. Two different measurement methods were used: small-angle measurements and a BS setup, which allowed for evaluation with the optics positioned perpendicularly to the incoming beam. The results from both setups well agreed with each other.

The DOEs and MLA3 showed the best results, with nearly 99% transmittance, likely due to the FS glass substrate, which has excellent optical properties. MLA1, made from PMMA, likely absorbed more light at the 405 nm wavelength. The metalens exhibited higher losses, likely due to backscattering. FZPs and GZPs performed worse because their zones were produced from chrome

coating, which acted as a mirror, reflecting all light that hit the non-transparent zones.

We simulated the multi-order behavior of an FZP lens, showing axial intensity distribution along the optical axis. Additionally, the intensity distribution at the first-order EFL was simulated and experimentally confirmed by measuring the beam intensity distribution with a beam profiler.

Both FZPs and GZPs exhibited multi-order behavior. GZPs, however, were able to suppress higher-order diffraction peaks by increasing the number of angular sectors, with the optimal number being 42, which almost completely suppressed higher-order modes.

The FCL beam was characterized using an M^2 beam analyzer, followed by the characterization of all focusing optics required for ML and MLA evaluation. The best M^2 results were achieved by the DOEs (D400 and D200), which did not significantly affect beam quality. In the case of D400, the beam quality even slightly improved, possibly due to the introduction of aberrations opposite to those inherent in the FCL beam or by suppressing higher-order diffraction through other mechanisms. The metalens also performed well. MLA3 showed great results that could have been even better with a larger lenslet aperture and longer EFL. FZPs failed the M^2 measurement due to strong higher-order diffraction peaks. GZPs with the highest number of angular sectors showed the best beam quality. MLA1 exhibited the worst beam quality, likely due to its short EFL, making alignment and collimation sensitive and complicated.

Finally, all micro-optics were evaluated using a SHWFS. Using similar optical setups to the M^2 factor measurements, we made a large number of measurements. The SHWFS allowed us to evaluate the strength and type of optical aberrations introduced by each ML.

Wavefront measurements showed results consistent with those from the M^2 factor setup. This time, the refractive microlenses showed the best optical quality, as this setup focused on collimated beam quality measurement. The DOEs and metalens performed similarly well, while the in-house fabricated FZPs and GZPs exhibited the worst optical performance. FZPs showed terrible beam qualityt as they do not contain a mechanism to suppress higher-order diffraction peaks. GZPs with a higher number of angular sectors showed better optical quality.

Overall, the DOEs D200 and D400 demonstrated the best optical performance, close to 99 % transmittance and minimal optical aberrations. The metalens performed similarly but had higher optical losses in the range of 40 %.

Refractive lenses remain a great traditional alternative, with more predictable performance. However, the short EFLs of the lenses tested made them highly sensitive to alignment, which may not be ideal for a moving nano-lithography setup. Custom MLAs with longer EFLs would be needed for such application.

Binary GZPs show potential in real-life applications as they showcase great focusing performance, with patterns having higher angular sectors effectively suppressing higher-order diffraction peaks. Additionally, the binary nature of GZPs makes their fabrication relatively straightforward using typical nano-lithography techniques.

Binary FZPs are generally unusable in most optical setups, due to lacking a higher-order diffraction suppression mechanism.

Finally, apertures demonstrated their usefulness in optical setups where spatial filtering is required, as they were able increase beam quality greatly.

6.1 Future work

This thesis provides an evaluation of various microlens types, but several directions are available for future work.

Using a reference laser with an M^2 value closer to 1 would simplify the interpretation of aberrations in the MLs. As the beam approaches ideal Gaussian behavior, any aberrations introduced by the microlenses would be more pronounced and the chance of MLs coincidentally compensating any inherent beam aberrations would be decreased.

GRIN lenses were originally planned for testing. Based on the literature they should be capable of supporting great beam quality. However, they seem to be limited to short EFLs. In addition to that, most GRIN technology is focused on the IR wavelength range, due to their applications in the telecommunications field. In the shorter wavelength range, closer to UV, the availability of such lenses seems to be more limited.

Future work should include testing the MLAs in multibeam setups to evaluate how these micro-optics function in the actual application case. The main parameters to be evaluated should include the repeatability of beam quality between lenslets, the divergence of collimated beams, and the stability of the beam (size, shape, position, quality) during Z-axis movement.

Finally, testing custom micro-optics with identical optical parameters, such as EFL, aperture size, and shape, would provide more conclusive results.

References

[1] M. Feldman, Nanolithography, Woodhead publishing, Philadelphia, 2014.

[2] L. Giuseppe et al., Multilevel pattern generation by GaN laser lithography: an application to beam shaper fabrication, Proceedings of the SPIE, vol. 6290, no. 62900A, 2006.

[3] H. Zappe, Fundamentals of Micro-Optics, Cambridge University Press, Cambridge, 2012.

[4] H. P. Herzig, Micro-Optics. Elements, Systems And Applications, CRC Press, London, 1997.

[5] R. Paschotta, Fresnel reflections, RP-Photonics, 2024: rp-photonics.com/fresnel_reflections.html

[6] W. B. Veldkamp, Overview of microoptics: past, present, and future, Proceedings of SPIE - The International Society for Optical Engineering, 1991.

[7] E. Hecht, Optics (5th Ed.), Pearson, London, 2017.

[8] B. D. Guenther, Modern Optics Simplified, Oxford university press, Oxford, 2020.

[9] C. Zhang et al., Fabrication of concave microlens arrays by local fictive temperature modification of fused silica, Optics Letters, vol. 42, no. 6, pp. 1093-1096, 2017.

[10] B.K. Lee et al., Replication of microlens arrays by injection molding, Microsystem Technologies, vol. 10, pp. 531-353, 2004.

[11] L. Sung-Keun Lee et al., A simple method for microlens fabrication by the modified LIGA process, Micromechanics and Microengineering, vol. 12, p. 334, 2002.

[12] F. L. Pedrotti et al., Introduction to Optics (3rd ed.), Cambridge University Press, Cambridge, 2017.

[13] B.E.A. Saleh et al., Fundamentals of Photonics (3rd Ed.), Wiley, Hoboken, 2019.

[14] R. Paschotta, Numerical Aperture, RP-Photonics, 2024: rp-photonics.com/numerical_aperture.html

[15] C.T. Pan et al., Hot embossing of micro-lens array on bulk metallic glass, Sensors and Actuators A: Physical, vol. 141, no. 2, pp. 422-431, 2008.

[16] H. Sankur et al., Fabrication of refractive microlens arrays, Proc. SPIE 2383, Micro-Optics/Micromechanics and Laser Scanning and Shaping, 1995.

[17] R. Voelkel et al., Fabrication of aspherical microlenses in fused silica and silicon, Proceedings of the SPIE, vol. 4440, pp. 40-43, 2001.

[18] A. Butkutė et al., Optimization of selective laser etching for assembly-free 3D micromechanic fabrication, Proceedings SPIE, Laser 3D Manufacturing VIII, vol. 1167715, 2021.

[19] A. Butkutė, Optimization of selective laser etching (SLE) for glass micromechanical structure fabrication, Optics Express, vol. 29, no. 15, pp. 23487-23499, 2021.

[20] R. Paschotta, Gradient-index Lenses, RP-Photonics, 2024: rp-photonics.com/gradient_index_lenses.html

[21] C. Ye et al., GRIN lens and lens array fabrication with diffusion-driven photopolymer, Optics Letters, vol. 33, no. 22, pp. 2575-2577, 2008.

[22] D. Gibson et al., IR GRIN Optics: Design and Fabrication, Proc. SPIE 10998, Advanced Optics for Imaging Applications: UV through LWIR IV, vol. 10181, no. 109980D, 2019.

[23] R. Paschotta, Wavefronts, RP-Photonics, 2024.: rp-photonics.com/wavefronts.html

[24] A. E. Siegman, Lasers, Sausalito, University Science Books, California, 1986.

[25] R. Paschotta, Shack–Hartmann Wavefront Sensors, RH-Photonics, 2024: rp-photonics.com/shack_hartmann_wavefront_sensors.html

[26] A. Vijayakumar et al., Design and Fabrication of Diffractive Optical Elements with MATLAB, SPIE, Washington, 2017.

[27] I. Cooper, Rayleigh-sommerfeld Diffraction Integral Of The First Kind Fresnel Zone Plate, 2024: d-arora.github.io/Doing-Physics-With-Matlab/mpDocs/op_rs_zones.pdf

[28] R. Paschotta, Zone Plates, RP-Photonics, 2024: rp-photonics.com/zone_plates.html

[29] V. Moreno et al., High efficiency diffractive lenses: Deduction of kinoform profile, American Journal of Physics, vol. 65, no. 6, 1997.

[30] M. M. Greve et al., The Beynon Gabor zone plate: a new tool for de Broglie matter waves and hard X-rays? An off axis and focus intensity investigation, Optics Express, vol. 21, no. 23, pp. 28483-28495, 2013.

[31] S. Deng et al., Carbon Nanotube Array Based Binary Gabor Zone Plate Lenses, Scientific Reports, vol. 7, 2017.

[32] Holo/Or, Diffractive optics lenses, 25 10 2020: holoor.co.il/diffractive-optics-lenses

[33] M. Kim et al., Metamaterials and imaging, Nano Convergence, vol. 22, no. 2, 2015.

[34] W. Tang et al., Metamaterial Lenses and Their Applications at Microwave Frequencies, Advanced Photonics Research, 2021.

[35] QuantumDesign, Optical metasurfaces & metalenses, MOXTEK: qd-europe.com/se/en/product/optical-metasurfaces-metalenses

[36] J. Lv et al., Metamaterial Lensing Devices, Molecules, vol. 24, no. 13, 2019.

[37] Metalens foundry service, MOXTEK: moxtek.com/optics-product/metalens-foundry

[38] A. Saleem et al., Fundamentals of light–matter interaction, Woodhead Publishing, Faisalabad, 2023.

[39] O. Stenzel, Light–Matter Interaction, Springer Nature, 2022.

[40] Understanding Neutral Density Filters, EdmundOptics: edmundoptics.com/knowledge-center/application-notes/optics/understanding-neutral-density-filters

[41] Laser: oxfordreference.com/display/10.1093/oi/authority.20110803100052312

[42] R. Paschotta, Laser Diodes, RP-Photonics, 2024: rp-photonics.com/laser_diodes.html

[43] H. Sun, Laser Diode Beam Basics, Manipulations and Characterizations, Springer, Pittsburgh, 2012.

[44] Elliptical beam circularization, Tholabs, 2024: thorlabs.com/images/TabImages/Elliptical_Beam_Circularization_Lab_Fact.pdf

[45] J. Vengelis, Laser Physics: Lecture notes, Vilniaus universiteto leidykla, Vilnius, 2023.

[46] R. Paschotta, Collimated Beams, RP_Photonics, 2024: rp-photonics.com/collimated_beams.html

[47] R. Paschotta, M2 Factor, 2024: rp-photonics.com/m2_factor.html

[48] G. Thériault, The beginner's guide to laser beam quality and M2 measurement, Gentec-EO, 2023: gentec-eo.com/blog/laser-beam-quality-measurement-m2

[49] R. Paschotta, Beam parameter product, RP-Photonics, 2024: rp-photonics.com/beam_parameter_product.html

[50] Scitec, M2 Factor (Quality Factor), 2024: scitec.uk.com/lasers/m2_factor.php

[51] M. Geoffrey-Axel, How can I measure the ellipticity of my laser beam?, Gentec-EO, 2024: gentec-eo.com/blog/how-can-i-measure-the-ellipticity-of-my-laser-beam

[52] Understanding Spatial Filters, EdmundOptics, 2024: edmundoptics.com/knowledge-center/application-notes/lasers/understanding-spatial-filters

[53] O. Wallner et.al., Minimum Length of a Single-Mode Fiber Spatial Filter, Journal of the Optical Society of America A, vol. 19, no. 12, pp. 2445-2448, 2002.

[54] G. P. Agrawal, Fiber-Optic Communication Systems (5th Ed.), Wiley, Rochester, 2021.

[55] Y. Beers, The theory of the optical wedge beam splitter, US Goverment printing office, Washington, 1974.

[56] Z. Cui, Nanofabrication. Priciples, capabilities and limits (3rd Ed.), Springer, Suzhou, 2024.

[57] R. Paschotta, Optical Aberrations, RP-Photonics, 2024: rp-photonics.com/optical_aberrations.html

[58] O. Axner, Analysis and design of optical systems (Part 3), Umeå universitet, Umeå, 2009.

[59] C. McAlinden et al., Mathematics of Zernike polynomials: a review, Clinical & Experimental Ophthalmology, vol. 39, no. 8, pp. 820-827, 2011.

[60] Y. Wang et al., Wave-front interpretation with Zernike polynomials, Original Manuscript, vol. 19, no. 9, pp. 1510-1518, 1980.

[61] Britannica, Aberrations, 2012: britannica.com/technology/aberration#ref61613

[62] Olympus, Astigmatism aberrations, 2016: olympus-lifescience.com/en/microscope-resource/primer/java/aberrations/astigmatism

[63] HyperPhysics, Astigmatism: hyperphysics.phy-astr.gsu.edu/hbase/geoopt/coma.html

[64] Comparison of optical aberrations, Edmund Optics: edmundoptics.com/knowledge-center/application-notes/optics/comparison-of-optical-aberrations

[65] LDM-XT Series, Lasos: lasos.com/en/laser-modules/ldm

[66] Vega Color laser power & energy meter, Ophir: ophiropt.com/en/f/vega-power-meter

[67] 300 mW UV-Silicon photodiode sensor, Ophir: ophiropt.com/en/f/pd300-uv-photodiode-sensor

[68] Edmund Optics beam profiler 4M, Edmund Optics: edmundoptics.com/p/edmund-optics-beam-profiler-4m/39992

[69] Considerations when using cylinder lenses, Edmund Optics: edmundoptics.co.uk/knowledge-center/application-notes/lasers/considerations-when-using-cylinder-lenses

[70] FC/APC Single Mode fibers, Thorlabs: thorlabs.com/newgrouppage9.cfm?objectgroup_id=6246

[71] TC25APC-405 SM Fiber coupler, Thorlabs: thorlabs.com/thorproduct.cfm?partnumber=TC25APC-405

[72] Y. Zhang, Fiber coupling of 405nm laser diode with μlens technology, Proc. SPIE 5272, Industrial and Highway Sensors Technology, 2004.

[73] Nikon Metrology NEXIV VMR-6555, Nikon: ryfag.ch/en/products/p/nikon-metrology-nexiv-vmr-6555

[74] Nikon, NEXIV VMR-6555, Nikon: web.archive.org/web/20240915233905/http://183.181.162.36/products/instruments/lineup/industrial/nexiv/large_stroke/vmr_6555/spec.htm

[75] PMMA microlens arrays, Thorlabs: thorlabs.com/newgrouppage9.cfm?objectgroup_id=14638

[76] Fused silica microlens arrays, Thorlabs: thorlabs.com/newgrouppage9.cfm?objectgroup_id=2861

[77] Ansys Zemax OpticStudio - comprehensive optical design software, Ansys: ansys.com/products/optics/ansys-zemax-opticstudio

[78] Photomask equipment products, Mycronic: mycronic.com/product-areas/photomask-equipment/Products

[79] MathWorks, MathWorks in Natic: mathworks.com/company/jobs/resources/locations/us-natick.html

[80] I. Cooper, Doing Physics with Python / Matlab, 2024: d-arora.github.io/Doing-Physics-With-Matlab

[81] I. Cooper, Fresnel zone plates - Irradiance pattern, 2024: github.com/D-Arora/Doing-Physics-With-Matlab/blob/master/mpScripts/op_rs_zones_z.m

[82] V. Kesaev, Gabor - Beynon zone plate with binary transmittance function, MATLAB Central File Exchange, 2024: mathworks.com/matlabcentral/fileexchange/125125-gabor-beynon-zone-plate-with-binary-transmittance-function

[83] Fused silica broadband dielectric mirrors, Thorlabs: thorlabs.com/newgrouppage9.cfm?objectgroup_id=139

[84] UV fused silica wedged windows, Thorlabs: thorlabs.com/newgrouppage9.cfm?objectgroup_id=8432

[85] MeetOptics, SHSLab Shack-Hartmann wavefront sensor, OptoCraft: meetoptics.com/detection-devices/wavefront-sensors/wavefront-sensor/s/optocraft/p/SHSCam%20HR3-130-GE%20UV

[86] SHSCam - UV/DUV sensor head overview (193 - 405 nm), Optocraft: optocraft.de/wp-content/uploads/2023/01/TS-SHSCam-Sensor-Head-Overview-WWW-221107.pdf

[87] Ophir, How to measure M-squared – two choices, Ophir, 2013: blog.ophiropt.com/how-to-measure-m-squared-two-choices

[88] G. Kostyuk et al., Microlens array fabrication on fused silica influenced by NIR laser, Applied Physics B, vol. 122, no. 99, 2016.

[89] R. Paschotta, Micro-optics, RP Photonics Encyclopedia, 2024.

Appendix

A.1 Zernike polynomials

Table A.1: Zernike Polynomials from radial orders n 0 to 6. Displayed with frequency m, and their relation to ocular aberrations [59].

n	m	Z_n^m	Z_n^m (p, θ)	Title
0	0	Z_0^0	1	Piston
1	−1	Z_1^{-1}	$4^{1/2} p\sin\theta$	Tilt (about x-axis)
1	1	Z_1^1	$4^{1/2} p\cos\theta$	Tilt (about y-axis)
2	−2	Z_2^{-2}	$6^{1/2} p^2\sin 2\theta$	Astigmatism (axis 45°, 135°)
2	0	Z_2^0	$3^{1/2} (2p^2 - 1)$	Spherical defocus
2	2	Z_2^2	$6^{1/2} p^2 \cos 2\theta$	Astigmatism (axis 0°, 90°)
3	−3	Z_3^{-3}	$8^{1/2} p^3 \sin 3\theta$	Trefoil (base on x-axis)
3	−1	Z_3^{-1}	$8^{1/2} (3p^3 - 2p) \sin\theta$	Coma (along x-axis)
3	1	Z_3^1	$8^{1/2} (3p^3 - 2p) \cos\theta$	Coma (along y-axis)
3	3	Z_3^3	$8^{1/2} p^3 \cos 3\theta$	Trefoil (base on x-axis)
4	−4	Z_4^{-4}	$10^{1/2} p^4 \sin 4\theta$	Tetrafoil
4	−2	Z_4^{-2}	$10^{1/2} (4p^4 - 3p^2) \sin 2\theta$	Secondary astigmatism
4	0	Z_4^0	$5^{1/2} (6p^4 - 6p^2 + 1)$	Spherical aberration
4	2	Z_4^2	$10^{1/2} (4p^4 - 3p^2) \cos 2\theta$	Secondary astigmatism
4	4	Z_4^4	$10^{1/2} p^4 \cos 4\theta$	Tetrafoil
5	−5	Z_5^{-5}	$12^{1/2} p^5 \sin 5\theta$	Pentafoil
5	−3	Z_5^{-3}	$12^{1/2} (5p^5 - 4p^3) \sin 3\theta$	Secondary trefoil
5	−1	Z_5^{-1}	$12^{1/2} (10p^5 - 12p^3 + 3p) \sin\theta$	Secondary coma
5	1	Z_5^1	$12^{1/2} (10p^5 - 12p^3 + 3p) \cos\theta$	Secondary coma
5	3	Z_5^3	$12^{1/2} (5p^5 - 4p^3) \cos 3\theta$	Secondary trefoil
5	5	Z_5^5	$12^{1/2} p^5 \cos 5\theta$	Pentafoil
6	−6	Z_6^{-6}	$14^{1/2} p^6 \sin 6\theta$	Hexafoil
6	−4	Z_6^{-4}	$14^{1/2} (6p^6 - 5p^4) \sin 4\theta$	Secondary tetrafoil
6	−2	Z_6^{-2}	$14^{1/2} (15p^6 - 20p^4 + 6p^2) \sin 2\theta$	Tertiary astigmatism
6	0	Z_6^{-0}	$7^{1/2} (20p^6 - 30p^4 + 12p^2 - 1)$	Secondary spherical aberration
6	2	Z_6^2	$14^{1/2} (15p^6 - 20p^4 + 6p^2) \cos 2\theta$	Tertiary astigmatism
6	4	Z_6^4	$14^{1/2} (6p^6 - 5p^4) \cos 4\theta$	Secondary trefoil
6	6	Z_6^6	$14^{1/2} p^6 \cos 6\theta$	Hexafoil

A.2 Expanded measurement results

A.2.1 Expanded small angle power measurement results

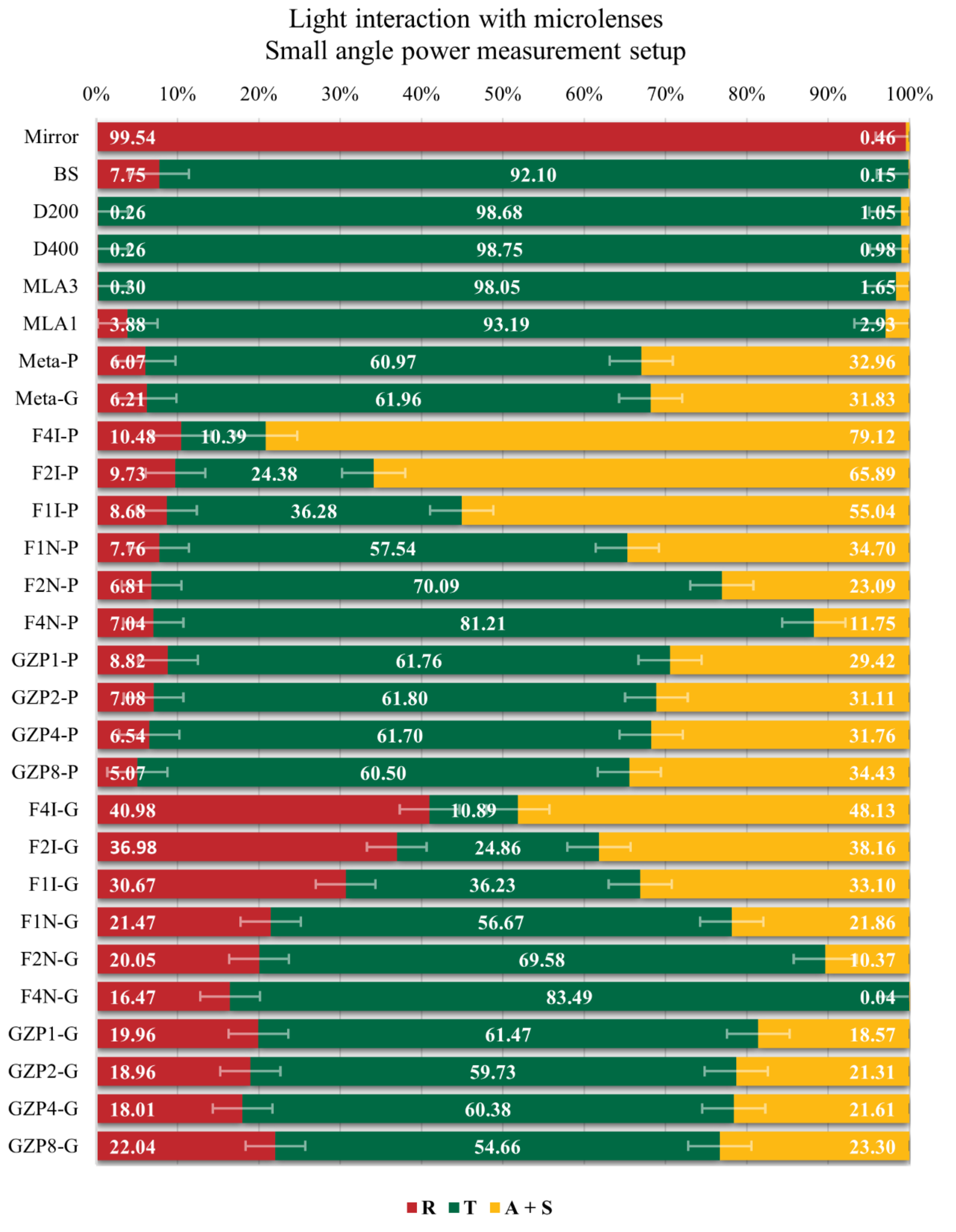

Figure A.1: Evaluated reflectivity, transmission, and absorption + back-scattered light coefficients (% values) for selected optics, based on small-angle power measurements. The results are expanded to include the XXX-P variant, with the ML oriented such that the pattern is the first surface hit by the laser beam, and the XXX-G variant, where the glass surface is the first to interact with the beam.

A.2.2 Expanded beam splitter power measurement results

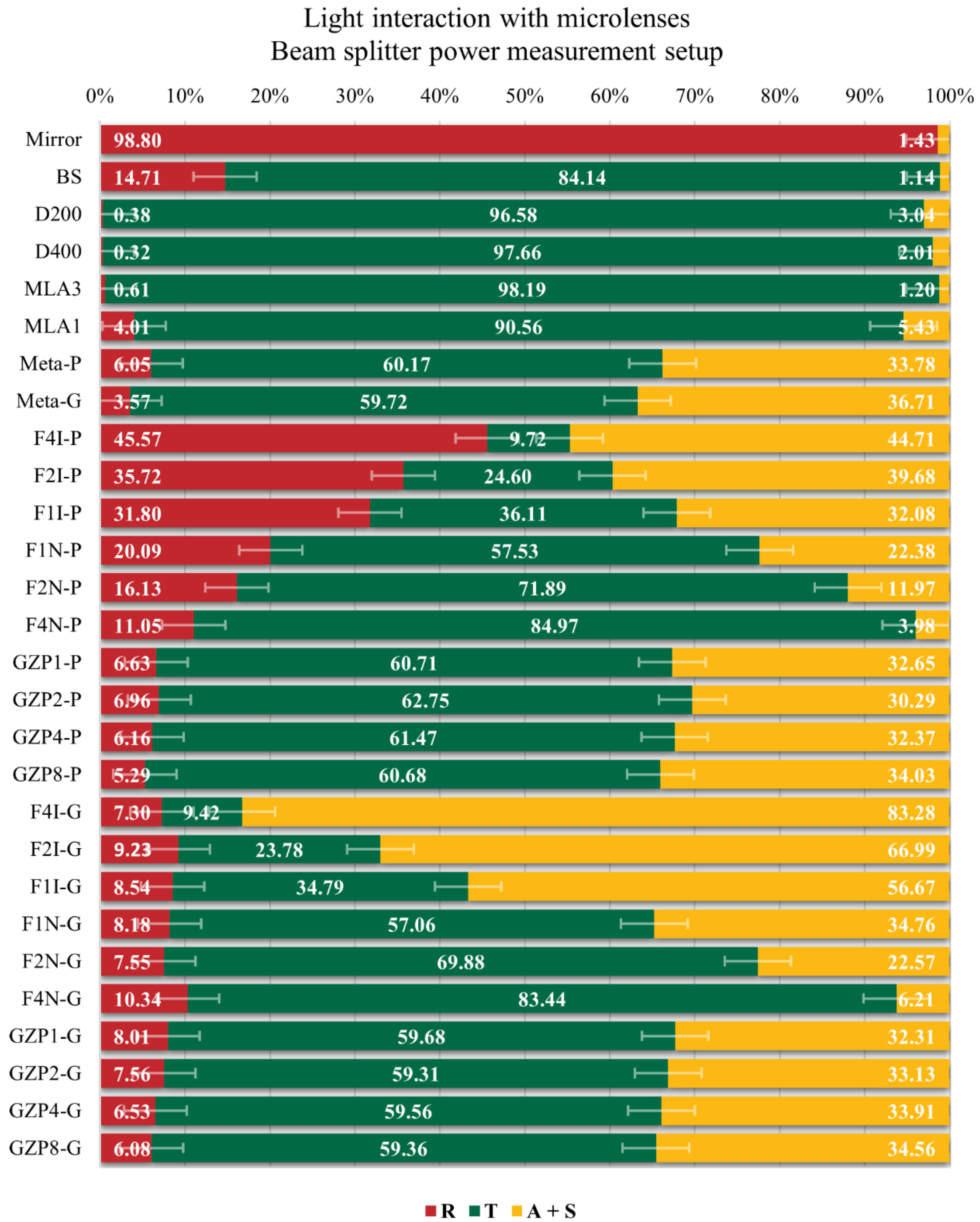

Figure A.2: Evaluated reflectivity, transmission, and absorption + back-scattered light coefficients (% values) for selected optics from beam splitter power measurements. The results are expanded to include the XXX-P variant, with the ML oriented such that the pattern is the first surface hit by the laser beam, and the XXX-G variant, where the glass surface is the first to interact with the beam.

A.2.3 Light interaction with microlenses. Expanded result comparison

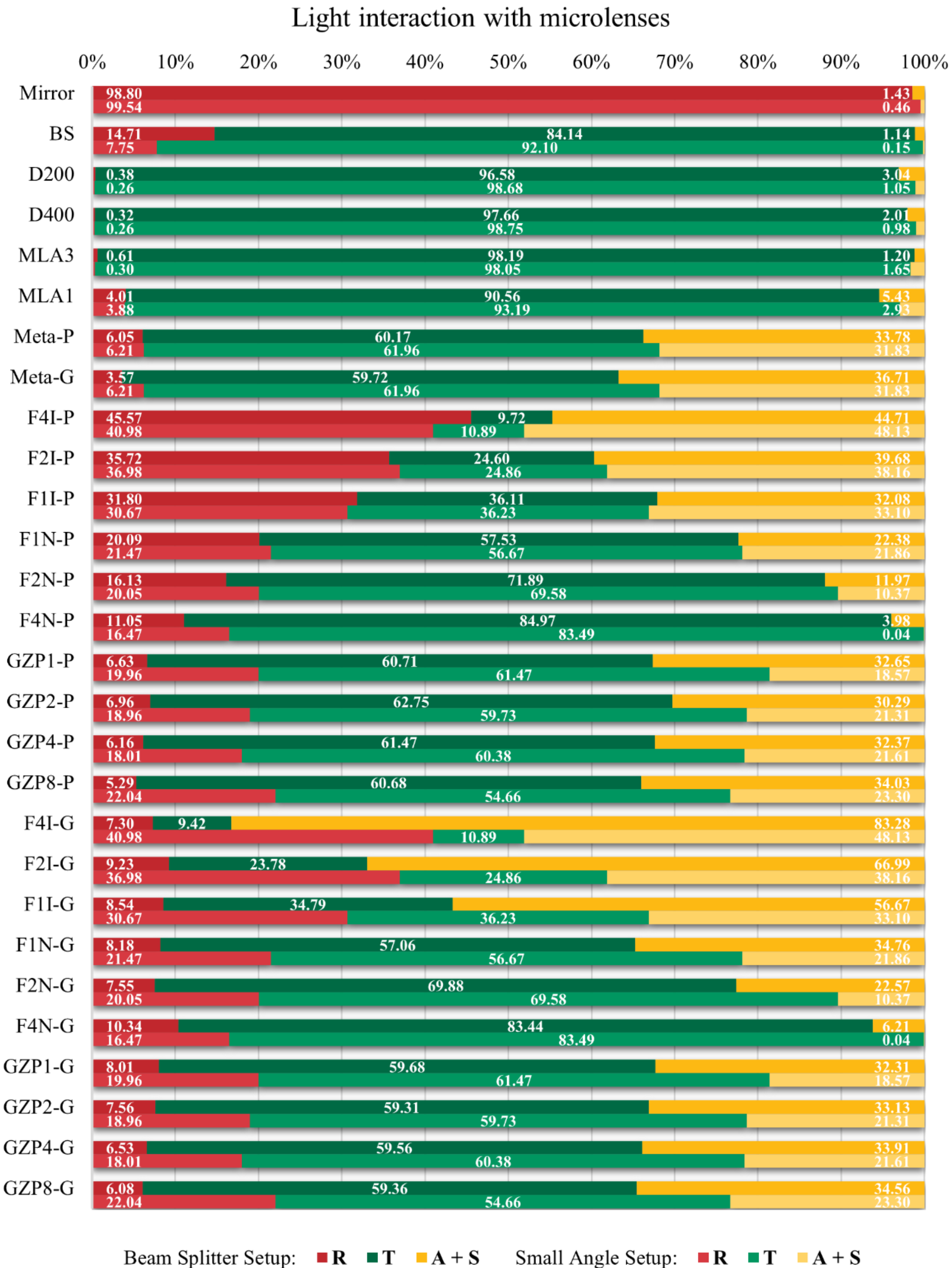

Figure A.3: Evaluated reflectivity, transmission, and absorption + back-scattering coefficients for selected optics. Clustered results with beam splitter setup results above, and small angle setup values below. The results are expanded to include the XXX-P variant, with the ML oriented such that the pattern is the first surface hit by the laser beam, and the XXX-G variant, where the glass surface is the first to interact with the beam.

A.2.4 M^2 factor measurements for focusing lenses

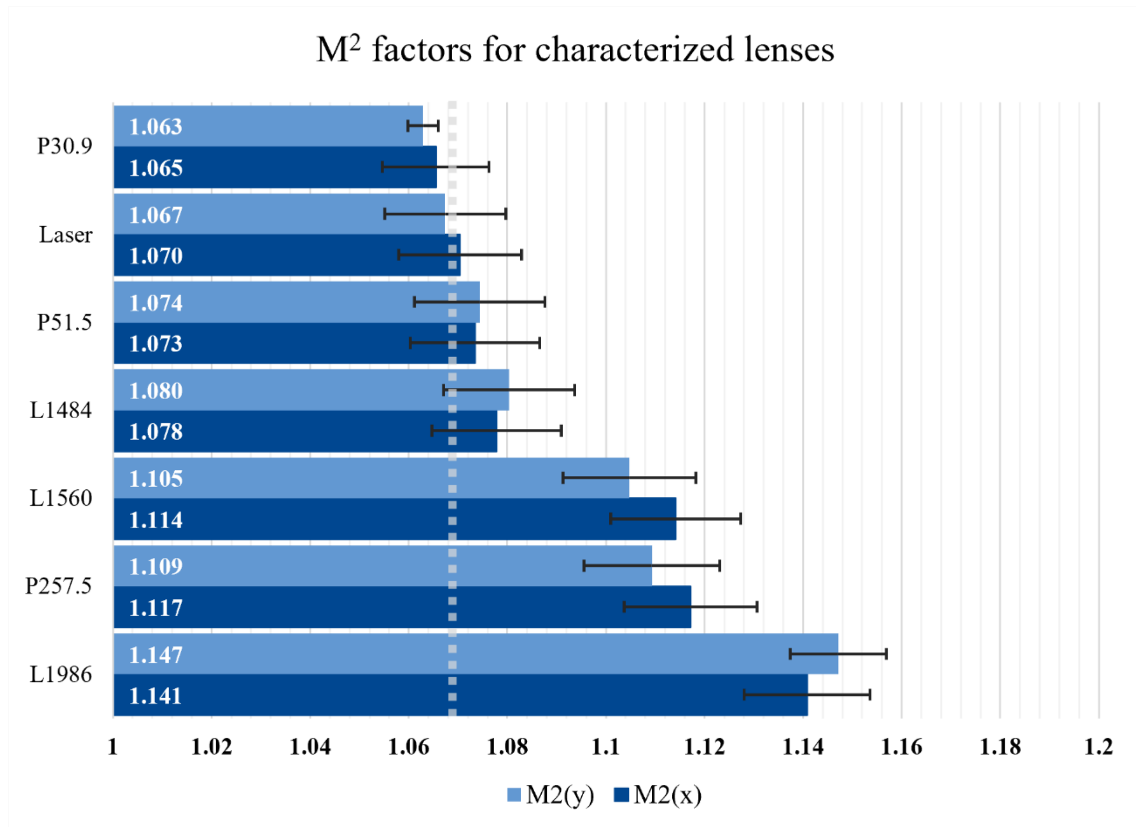

Figure A.4: M^2 factors for focusing lenses. The dashed line stands for the average M^2 factor of 1.069 for the LD source.

A.2.5 Wavefront measurements

Zernike polynomial with amplitude coefficients

	Zernike	Residual	C0	C1	C2	C3	C4	C5	C6	C7	C8	C9	C10	C11	C12	C13	C14	C15
Laser	0.004	0.005	-0.024	0.020	-0.520	0.191	0.019	0.048	0.012	-0.027	-0.012	0.005	-0.001	0.001	-0.001	-0.002	0.000	0.001
MLA3	0.005	0.004	-0.104	0.176	-0.451	0.516	-0.001	0.007	0.007	-0.001	0.004	0.008	-0.001	-0.002	-0.001	0.001	-0.002	-0.001
MLA1	0.009	0.006	-0.512	0.646	-1.470	0.436	0.023	0.007	-0.013	-0.004	0.001	0.009	-0.006	0.003	0.003	0.002	0.000	0.000
D400	0.011	0.003	-0.101	0.034	-0.284	0.755	0.019	-0.014	-0.015	-0.011	-0.006	-0.004	-0.002	0.006	-0.001	0.002	0.001	-0.001
Meta	0.012	0.009	-0.034	0.124	-0.456	2.210	0.006	-0.002	-0.009	-0.001	-0.004	-0.003	0.003	0.006	0.006	-0.004	0.002	0.003
D200	0.013	0.007	-0.003	0.079	-0.379	0.045	0.022	-0.020	0.009	-0.013	-0.014	0.004	0.001	0.008	-0.003	-0.012	0.004	0.000
F1I	0.021	0.025	-0.004	0.055	-0.738	0.014	0.008	0.000	-0.023	-0.017	-0.033	0.015	0.003	-0.004	0.013	0.026	0.012	0.000
GB4	0.080	0.074	-0.020	-0.116	-0.075	-0.009	0.125	0.060	-0.034	-0.017	0.015	-0.008	-0.009	-0.006	-0.011	0.120	-0.031	0.079
GB8	0.092	0.072	-0.026	-0.111	-0.347	-0.041	0.091	-0.055	-0.146	0.041	-0.009	0.037	-0.025	0.025	-0.048	0.140	-0.086	0.090
F4N	0.134	0.097	-0.061	-0.430	-0.206	-0.053	0.055	-0.071	-0.014	-0.226	-0.075	0.036	0.151	0.037	-0.026	-0.023	0.015	0.201
GB2	0.218	0.112	0.037	0.588	-0.498	0.151	0.326	-0.260	0.123	0.231	0.085	0.238	-0.368	0.006	-0.198	0.135	-0.212	0.092
F2N	0.225	0.202	-0.032	0.178	-1.547	0.835	-0.419	0.048	-0.078	-0.112	-0.024	0.121	-0.179	0.014	-0.284	-0.009	-0.292	-0.174
F4I	0.271	0.169	-0.264	-0.870	-1.377	0.781	0.002	-0.006	-0.240	0.067	0.484	-0.008	-0.011	-0.007	0.047	0.212	-0.110	-0.231
GB1	0.283	0.194	-0.023	-0.048	-0.590	-0.015	0.146	0.017	-0.460	0.467	0.052	0.139	0.151	0.036	-0.026	0.388	-0.252	0.048
F2I	0.516	0.247	-0.072	-1.341	-1.637	0.691	-0.131	0.534	-0.748	-0.543	0.932	0.207	-0.024	-0.352	0.053	-0.108	-0.448	-0.081
F1N	1.317	0.306	-1.292	2.421	0.252	-1.749	-2.718	0.626	2.858	0.834	0.100	2.099	1.428	-0.886	-0.065	1.916	-0.425	0.501

Figure A.5: Measured general Zernike polynomial (RMS) values, with residual part, as well as Zernike polynomial amplitude coefficient values for several types of aberrations.

TRITA-SCI-GRU 2024:384
Stockholm, Sweden 2024

www.kth.se